Journal of Environmental Chemical Engineering 13 (2025) 118929

Contents lists available at ScienceDirect

Journal of Environmental Chemical Engineering

journal homepage: www.elsevier.com/locate/jece

Characteristics of gas-solid products and sodium-chloride fixation mechanism of synergistic pyrolysis of low-rank coal and low-grade phosphorite: Experimental and molecular dynamics simulation

Zhihua Tian [1], Bin Zhang [1], Ying Zhao [1], Qinhui Wang [*], Yingchi Chen, Ruiqing Jia, Yufei Liu, Dong Ma

State Key Laboratory of Clean Energy Utilization, Zhejiang University, Hangzhou 310027, China

ARTICLE INFO

Keywords:
Fluidized bed
Low-rank coal
Pyrolysis
Additives
Molecular dynamics

ABSTRACT

To improve the quality of low-rank coal pyrolysis products and mitigate equipment corrosion caused by sodium/chlorine (Na/Cl) release, this study investigated the effects of phosphorite addition on the product characteristics and reaction mechanism of the fluidized bed co-pyrolysis of Xinjiang Naomaohu coal (NM) and Hami coal (HM). The experimental results showed that the addition of phosphorite increased the char yield and cold gas efficiency. Air thermogravimetric experiments revealed that the addition of phosphorite improved the combustion performance of the char. Raman, XRD, and BET analyses revealed that phosphorite altered the microstructure and pore properties of the char. Phosphorite reacts with the Na/Cl in coal to form stable compounds, which inhibited the volatilization of Na/Cl. Molecular dynamics simulations show that apatite exhibits stronger adsorption capacity for Na^+ /Cl^- than quartz sand and austenitic steel. Recycling phosphorite from pyrolysis and using it in a carbothermal reduction process to produce yellow phosphorus effectively improves conversion ratio. This integrated approach not only optimizes pyrolysis product quality and mitigates corrosion risks but also provides an economically viable strategy for the synergistic utilization of low-rank coal and low-grade phosphorite in industrial applications.

Introduction

Due to the rapid globalization of the world economy, the global demand for fossil fuels [1–3], particularly coal resources, remains substantial. To enhance the utilization value of coal resources, optimizing their mining techniques and utilization patterns is of critical importance [4–12]. Coal remains the most widely used energy source globally, accounting for over one-third of the total electricity supply [13–16]. Low-rank coal refers to coal at an early coalification stage. It typically has high moisture and ash contents, high volatile matter and a low heating value. Given its extensive reserves and lower mining costs [17], low-rank coal plays a crucial role in national energy security, necessitating the advancement of clean utilization technologies [18–20]. However, rough use of coal resources leads to excessive carbon dioxide (CO_2) and particulate emissions [21–23], prompting worldwide efforts to develop cleaner utilization strategies. Meanwhile, the Na/Cl released by the huge reserves of high-Na and high-Cl coal during the thermal utilization process will cause contamination and corrosion of the heating surface. Solving this problem is conducive to improving its utilization value, which is also one of the key issues to be solved in this study. Pyrolysis offers an effective approach to coal utilization, yielding tar, char, and light gases as primary products [24]. Char, characterized by low volatility, high fixed carbon content, high reactivity, high electrical resistivity, and a well-developed pore structure [25], is widely applied in metallurgy, chemical engineering, and adsorption processes. Meanwhile, pyrolysis gas, a directly usable fuel, holds high value for industrial and civil energy supply. Research efforts have thus been directed toward optimizing pyrolysis processes to enhance both product yield and quality [26].

To improve the value of pyrolysis products and reduce process costs, many studies have investigated process modifications and additive incorporation. Wang et al. [27] reported that red mud facilitates Fe_2O_3-catalyzed reactions, enhancing tar and gas quality. Pan and Serageldin [28] demonstrated that calcium chloride and calcium acetate

* Corresponding author.
E-mail address: qhwang@zju.edu.cn (Q. Wang).
[1] These authors contributed equally to this work.

https://doi.org/10.1016/j.jece.2025.118929
Received 16 May 2025; Received in revised form 10 August 2025; Accepted 24 August 2025
Available online 25 August 2025

lower the activation energy required for lignite pyrolysis, accelerating reaction rates. Other studies have explored the role of calcium oxide (CaO), calcium hydroxide ($Ca(OH)_2$), calcium nitrate ($Ca(NO_3)_2$), calcium chloride ($CaCl_2$), calcium acetate ($Ca(Ac)_2$) and calcium carbonate ($CaCO_3$), showing that these compounds increase gas yields while reducing tar formation [29–33]. Phosphorite, a critical resource for agriculture, energy, and chemical industries [34,35], is primarily processed via wet or thermal phosphoric acid production [36–39]. However, 93 % of phosphorite resources of China are medium-grade and low-grade phosphorite, and high-grade phosphorite with P_2O_5 accounting for more than 30 % account for very little [40]. Making full use of medium-grade and low-grade phosphorite resources is of great significance. Compared with the calcium-containing additives used in previous studies, phosphorite also has plenty of calcium-containing compounds (such as CaO, $Ca_5(PO_4)_3F$) and other alkali metal oxides, which can participate in pyrolysis to improve the quality of the products.

The synergistic pyrolysis process of low-rank coal and low-grade phosphorite selected in this study is mainly based on the following theoretical and practical basis. High-sodium low-rank coal has a high Na/Cl content. The release of Na/Cl will cause severe corrosion, resulting in a significant increase in operating costs. Although the additives such as pure CaO and $Ca(OH)_2$ used in existing studies can partially fix Na/Cl, they are expensive and difficult to recover, which is not conducive to industrial promotion. Due to the huge reserves of low-grade phosphorite in China, its rich calcium-based compounds such as CaO and $Ca_5(PO_4)_3F$ can combine with Na/Cl through chemical reactions at 500–900 °C to form stable sodium phosphate and chloride salts [41,42], which play a similar calcium-based catalytic and fixation role in pyrolysis. Meanwhile, the participation of phosphorite in the pyrolysis process is equivalent to pretreatment. The pretreated phosphorite has higher conversion ratio in the process of carbothermal reduction to produce yellow phosphorus [43], which solves the problem of post-treatment of additives. Fluidized bed pyrolysis has good gas-solid heat transfer and mixing characteristics, and is suitable for large-scale application [44,45]. Combining various characterization methods with molecular dynamics simulation, the mechanism of the influence of phosphorite on the properties and structure of char, pyrolysis gas composition, and Na/Cl release can be analyzed at the microscopic level, providing theoretical support for optimizing process parameters and additive ratios. Therefore, this study hopes to explore a feasible path for the coordinated utilization of coal- phosphorite resources in an economical and environmentally friendly way.

Our previous research explored the effects of phosphorite on the yield of pyrolysis products from a single type of coal, focusing on its effects on the migration of different forms of Na/Cl in coal during pyrolysis. To determine the universality of phosphorite effects, this study used two different high-sodium, low-rank coals for testing and further explored its effects on pyrolysis gas composition and the microscopic properties and structure of char. Furthermore, this study used molecular dynamics simulations to analyze the mechanism by which phosphorite is more effective in fixing Na/Cl. Building on this previous research, this study proposed a process flow for practical industrial production.

In order to alleviate the equipment corrosion problem caused by the release of Na/Cl during the pyrolysis of high-sodium coal, this experiment used a fluidized bed reactor to study the effect of phosphorite on the pyrolysis products and Na/Cl release characteristics. The effects of different temperatures and phosphorite dosages on the char yield and pyrolysis gas components were explored. The char was characterized by combining thermogravimetric, XRD, Raman and BET tests, and the effect of phosphorite on the physical and chemical properties of char was discussed. The effect and mechanism of phosphorite on the release of Na/Cl during pyrolysis were explored through experiments and molecular dynamics simulations. The phosphorite involved in pyrolysis was recovered and used for carbothermal reduction reaction to prepare yellow phosphorus, and the effect of pyrolysis on the recycled phosphorite was explored.

The main innovation of this study is that a new process technology route is proposed, using lower-cost phosphorite to replace traditional high-purity calcium-based additives, and for the first time systematically exploring the role and resource potential of phosphorite in coal-phosphorite synergistic pyrolysis. The microscopic effect and mechanism of phosphorite on pyrolysis products are also explored. This research can not only provide an economically feasible solution for the industrial clean utilization of high-sodium low-rank coal, but also provide pre-treated raw materials for the production of downstream phosphorus products, forming an industrial linkage with phosphorus chemical industry.

Experimental

Materials and equipment

This study used Naomaohu coal (NM) and Hami coal (HM) from Xinjiang province, whose industrial, elemental, and calorific value analysis results are presented in Table 1. The phosphorite used in this experiment was sourced from Hubei province, with a P_2O_5 content of 22.31 %, classified as low to medium-grade. Using the Aeska mixture melt-potassium thiocyanate titration method as specified in GB/T 3558–1996 [46], the total Cl content in NM and HM was found to be 3944 μg g^{-1} and 4316 μg g^{-1}, respectively. Based on prior research [47], 1 g samples of NM and HM were digested at 260 °C for 60 min using the WX-7000HP microwave digestion system (Purchasing area: China). The digestion mixture consisted of 5 mL nitric acid (HNO_3), 2.5 mL hydrochloric acid (HCl), 1 mL hydrofluoric acid (HF), and 0.3 mL hydrogen Peroxide (H_2O_2) (Purchasing area: China). The Na content in the samples was measured by Agilent 5110 (OES) (Purchasing area: America) as 5127 μg g^{-1} and 3408 μg g^{-1}, respectively. According to the criteria set by MT/T 1074–2007 [48] and GB/T 20475.2–2006 [49], coal with Na content above 0.5 % is considered high-sodium coal and between 0.3 % and 0.5 % is medium-sodium, while Cl content above 0.3 % is considered high-chlorine coal. Based on the Na and Cl content, NM is classified as high-sodium, high-chlorine coal and HM is classified as medium-sodium, high-chlorine coal. The Na and Cl content in the char was determined using the same method as for the coal samples.

The reactor used in this experiment is a small fluidized bed reactor (Purchasing area: China), as shown in Fig. 1. The reactor is divided into a preheating section (5500 mm in length) and a main reaction section (30 mm diameter, 700 mm length). The reactor is constructed from austenitic steel, which can operate stably at temperatures up to 1000 °C for up to 8 h. The temperature distribution within the reactor is uniform, with temperature differences between the dense phase, dilute phase, and coal feed sections kept within 20 °C. Preliminary experiments found that the fluidization effect is best when the particle size of the heat carrier quartz sand is 0.25–0.35 mm and the particle size of the coal is 0.90–2.00 mm. Therefore, the carrier gas is argon (Ar), and 150 g of quartz sand with a particle size of 0.25–0.35 mm is used as the bed material (Purchasing area: China). The coal samples, sieved to a size of 0.90–2.50 mm, are introduced via a screw feeder, and 15 g of coal is added each time for pyrolysis once the temperature has stabilized. Phosphorite is mechanically mixed with coal before being introduced into the reactor. Preliminary experiments have found that smaller phosphorite particle size can increase the specific surface area and thus adsorb more Na and Cl. In order to ensure that the phosphorite has good adsorption capacity and can quickly separate from char and quartz sand, the particle size of the phosphorite is selected to be 0.43–0.70 mm. After the experiment, the char was first separated with a 0.7 mm sieve, and then the phosphorite and quartz sand were separated with a 0.35 mm sieve, so that the char and phosphorite can be characterized and followed up with experiments. The tail of the experimental device is connected to the filter element and the air collection bag in sequence to capture the pyrolysis gases. Preliminary tests [50–52] showed that the critical fluidizing air flow rate for the bed height of 14.39 cm was

Table 1
Industrial, elemental, and calorific value analysis results of NM and HM.

Sample	Industrial analysis (wt%)				Elemental analysis (wt%)					Calorific value (J g^{-1})
	M_{ad}	A_{ad}	V_{ad}	FC_{ad}	C_{ad}	H_{ad}	N_{ad}	S_{ad}	O_{ad}	
NM	6.18	11.32	31.46	50.92	60.61	3.78	0.95	0.24	16.27	22436
HM	4.50	6.91	36.03	52.56	67.87	4.46	1.06	0.30	14.90	26763

M_{ad}: Moisture, air dried basis; A_{ad}: Ash content, air dried basis; V_{ad}: Volatile matter, air dried basis; FC_{ad}: Fixed carbon, air dried basis; C_{ad}: Carbon content, air dried basis; H_{ad}: Hydrogen content, air dried basis; N_{ad}: Nitrogen content, air dried basis; S_{ad}: Sulfur content, air dried basis; O_{ad}: Oxygen content, air dried basis.

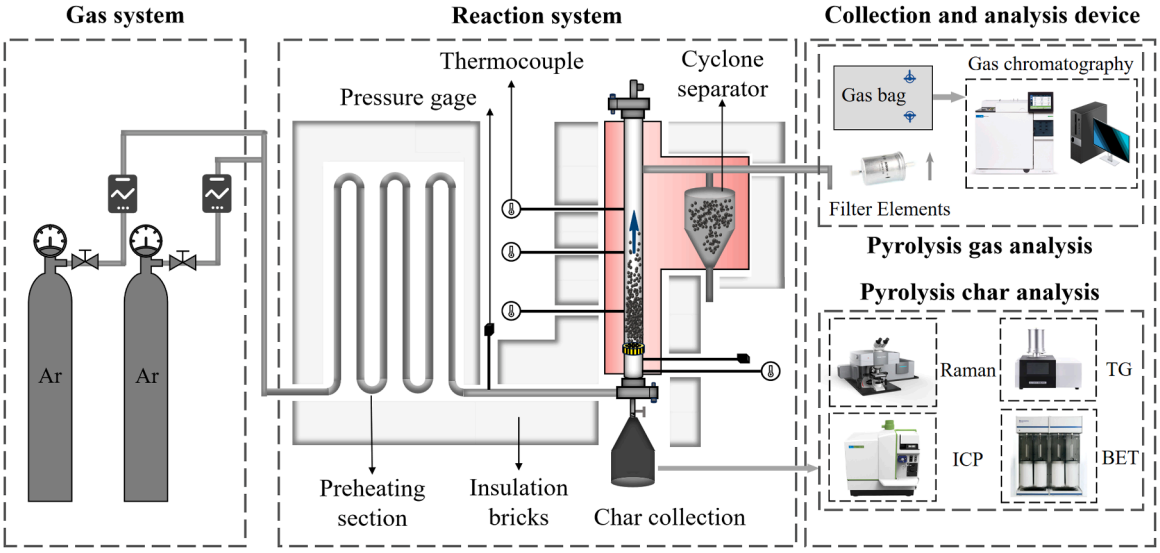

Fig. 1. A small fluidized bed reactor for coal-phosphorite co-pyrolysis.

3.0 L min^{-1}. Therefore, the carrier gas flow rate in this experiment was set to 4.2 L min^{-1}, which was 1.5–2 times the critical fluidizing air flow rate. 500 °C, 600 °C, 700 °C, 800 °C, and 900 °C were selected as pyrolysis temperatures, and multiple preliminary experiments were carried out. The flue gas components were measured using a synchronous online flue gas analyzer. The results showed that when pyrolyzed at various temperatures, the longest reaction time for the pyrolysis gas components to no longer change in all working conditions was 6 min. Meanwhile, the mass of char changed very little after the pyrolysis time exceeded 6 min. This result shows that the pyrolysis reaction is basically completed when the pyrolysis time is 6 min. Therefore, considering the time cost and experimental accuracy, the pyrolysis time was selected as 6 min in this experiment.

The pyrolysis gas was collected and analyzed using an Agilent 8890 gas chromatograph (Purchasing area: America). Argon is inert in our pyrolysis conditions. Therefore, all Argon in the product gas originates from the carrier gas. Gas volume was determined using the Ar tracer method, and the gas mass M_{gas} was calculated using **Formula (1)**. After the reaction, the bottom valve of the reactor was opened to discharge the material, which was then screened to separate the quartz sand, char, and phosphorite. The mass of the char was recorded as M_{Char} (g), and the char yield η_{Char} (%) was calculated using **Formula (2)**.

$$M_{gas} = \frac{M_{Ar}}{N_{Ar}} \cdot (1 - N_{Ar}) = \frac{V_{Ar} \cdot t \cdot c \cdot M_r}{V_m \cdot N_{Ar}} \cdot (1 - N_{Ar}) \quad (1)$$

$$\eta_{Char} = \frac{M_{Char}}{M_{Coal}} \times 100\% \quad (2)$$

$$\eta_{Na} = \frac{n_1 \cdot M_{char}}{n_{Na} \cdot M_{coal}} \quad (3)$$

$$\eta_{Cl} = \frac{n_2 \cdot M_{char}}{n_{Cl} \cdot M_{coal}} \quad (4)$$

$$\eta = \frac{M_{PH} x_{PH} - M_{Ash} \alpha_{Ash}}{M_{PH} x_{PH}} \times 100\% \quad (5)$$

In the formula, V_{Ar} denotes the volume of Ar (L), N_{Ar} represents the mass fraction of Ar, t is the pyrolysis time (min) , c is the flow rate of the inlet gas (L min^{-1}), Vm is the standard molar volume (22.4 L mol^{-1}), and Mr is the relative atomic mass of Ar (40 g mol^{-1}). The concentrations of CO, CO_2, CH_4, and H_2 in the pyrolysis gas can be calculated by multiplying the gas mass by the respective component mass fractions, which are measured using a gas chromatograph. The Na/Cl release ratios during pyrolysis can be determined using **Formula (3)** and **Formula (4)**, respectively. In the formula, n_{Na} (μg g^{-1}) indicates the relative sodium content in the coal, n_{Cl} (μg g^{-1}) represents the chlorine content in the coal, n_1 (μg g^{-1}) refers to the sodium content in the char, and n_2 (μg g^{-1}) corresponds to the chlorine content in the char. The phosphorite, after screening, is collected and ground to a particle size of less than 0.15 mm. It is then mixed with coal powder and placed in a fixed bed made from alumina for reduction. Following previous studies [53,54] on the thermal reduction of phosphorite, about 15 g of phosphorite is weighed for each sample, with the mass recorded as M_{PH} (g). Using the P_2O_5 content of the phosphorite as a benchmark, coal powder is added with a carbon excess factor of 1.6, and high-purity SiO_2 is added with a silicon-calcium molar ratio of 2.0. Before the experiment begins, the weighed phosphorite, coal, and silica need to be mechanically stirred until they are completely mixed. Before heating a fixed bed, nitrogen gas with a flow rate of 100 L h^{-1} is introduced for purging. In this experiment, a fixed bed heating rate was set at 10 °C min^{-1}. After reaching the set temperature, the nitrogen flow rate was adjusted to 500 L h^{-1} and the mixed sample was added. After the reaction, the slag is removed, weighed, and recorded as M_{Ash} (g). The P_2O_5 content of the slag is

measured according to GB/T 1871.1–1995 [55] and recorded as α_{Ash}, while the P_2O_5 content of the phosphorite is noted as α_{PH}. The conversion ratio of the phosphorite, η (%), can be calculated using **Formula (5)**.

Methods

Combustion characteristics of char are typically represented by the ignition temperature (θ_i) and burnout temperature (θ_b) [56]. The thermogravimetric experiments of char were conducted using the Mettler TGA/DSC 3 + automatic sampling synchronous thermal analysis system (Purchasing area: Switzerland) to obtain TG/DTG curves. The ignition temperature is defined as the temperature at which the reaction rate reaches 1 % min^{-1} at the start of the combustion process, while the burnout temperature is the temperature at which the reaction rate reaches 1 % min^{-1} at the end of combustion. A lower ignition temperature indicates better ignition performance, and a lower burnout temperature signifies better burnout performance [57]. The combustion characteristics of char were further analyzed using the combustibility index (C), stability index (G), and comprehensive combustion characteristics index (S), calculated using **Formula (6) - (8)**. In these formulas, $(dm/dt)_{max}$ is the maximum reaction rate (% min^{-1}), θ_{max} is the temperature corresponding to the maximum reaction rate, and $(dm/dt)_{meam}$ is the average combustion rate (% min^{-1}). A higher combustibility index (C) indicates better flammability [58], while a higher stability index (G) indicates more stable combustion behavior [59]. The comprehensive combustion characteristics index (S) reflects both ignition and burnout performance, with higher values indicating better combustion characteristics [60].

$$C = \frac{(dm/dt)_{max}}{T_i^2} \tag{6}$$

$$G = \frac{(dm/dt)_{max}}{T_i \cdot T_{max}} \tag{7}$$

$$S = \frac{(dm/dt)_{max} \cdot (dm/dt)_{mean}}{T_i^2 \cdot T_b} \tag{8}$$

To explore the influence of different pyrolysis conditions on the microstructure of char, various characterization techniques including XRD, Raman, and BET tests were applied. XRD analysis was performed using the Rigaku SmartLab SE X-ray diffractometer (Purchasing area: Japan), employing a copper target X-ray tube with a voltage of 40 kV, Ka radiation λ = 0.15406 nm, scanning speed of 2 ° min^{-1}, and a scan range from 10° to 80°. Since char is a solid product formed after coal is pyrolyzed at medium or low temperatures, its structure is mainly amorphous carbon and has a complex composition. JCPDS cards are mainly for single, well-crystallized phases. The disorder of char leads to the lack of a clear crystal structure, so char does not have a dedicated JCPDS number. In order to study the characteristics of char, this study calculated the microcrystal parameters and compared the structural morphology of char under different working conditions, so as to analyze the effects of temperature and phosphorite on char. *Jade* software was used to perform peak fitting on the XRD data to obtain the peak positions and half-height widths of the 002-peak and the 100-peak. According to the Scherrer formula and Bragg formula [61,62], the obtained characteristic parameters are substituted into **Formula (9) - (11)** to calculate the characteristic parameters of the microcrystalline structure of the char. In these formulas, d_{002} is the distance between the aromatic monolayers in the char, λ is the wavelength of the incident X-ray (0.15406 nm), while θ_{002} and θ_{100} are the grazing angles. The 002 peak represents the degree of orientation of the aromatic layers in the crystallite in space. The higher and narrower the peak, the better the orientation of the layers [63]. The 100 peak can reflect the degree of condensation of the aromatic ring (the size of the aromatic lamellae). The higher and narrower the 100 peak is, the larger the lamellae diameter is (the higher the degree of condensation of the aromatic nucleus) [64]. L_a is the size of the crystallite parallel to the aromatic lamellae, L_c is the stacking height of the crystallites perpendicular to the aromatic lamellae, K_1 and K_2 are the form factors (K_1=0.89, K_2=1.84), while β_{002} and β_{100} are the half-height widths of the diffraction peaks.

$$d_{002} = \frac{\lambda}{(2 \sin \theta_{002})} \tag{9}$$

$$L_c = \frac{K_1 \cdot \lambda}{(\beta_{002} \cdot \cos \theta_{002})} \tag{10}$$

$$L_a = \frac{K_2 \cdot \lambda}{(\beta_{100} \cdot \cos \theta_{100})} \tag{11}$$

Raman spectroscopy is highly sensitive to structural ordering in carbonaceous materials and is therefore widely used to characterize coal/char microstructure [65,66]. In this experiment, a Raman spectrometer model Horiba LabRAM HR Evolution (Purchasing area: Japan) was used to analyze the pyrolysis char. The spectral resolution was 1 cm^{-1} and the test wavelength was 514 nm. The Raman spectrum in the wavenumber range of 800–1800 cm^{-1} was fitted into 10 Gaussian peaks using *PeakFit* software [67]. According to previous studies [68,69], G_r peak, V_L peak, and V_r peak are the peaks in the Raman spectrum that reflect specific ordered structures or characteristic vibrations. The S peak can reflect the structural system of aliphatic groups, the G peak can reflect the degree of graphitization of sp^2 carbon, and the D peak is mainly related to defects or disordered structures. Based on the obtained data, the values of $I_{Gr+VL+Vr}/I_D$, I_G/I_D, I_G/I_{total}, and I_S/I_G can be calculated to understand the effects of different pyrolysis conditions on the microstructure of char.

BET tests were conducted using a Micromeritics ASAP 2460 (Purchasing area: America) to determine the specific surface area and porosity of char under various pyrolysis conditions. These tests provided insights into how different pyrolysis conditions influence the pore development of char. In each experiment, the sample was first degassed at 300 °C for 7 h under vacuum conditions to remove adsorbed moisture and impurities on the sample surface. Isothermal N_2 adsorption–desorption measurements were performed at 77 K. These tests provided insights into how different pyrolysis conditions influence the pore development of char.

Molecular dynamics simulation

In this study, *Materials Studio* software was utilized to simulate and calculate the interaction of Na^+/Cl^- with various materials through molecular dynamics simulations using the spin-unrestricted *DFT* method implemented in the *DMol*^{3} code [70]. The electronic exchange and correlation effects were modeled with the Perdew-Burke-Ernzerhof (PBE) generalized gradient approximation (GGA), and a double numerical plus polarization (DNP) basis set was used [71]. The convergence tolerances for energy changes, maximum forces, and maximum displacements were set to 2.0×10^{-5} Ha, 0.004 Ha $Å^{-1}$, and 0.005 Å, respectively. A 3 × 3 × 1 Monkhorst-Pack grid was used for Brillouin zone integration [72], and a 15 Å vacuum layer was added between periodically repeated slabs to avoid slab-slab interactions. The main aim of this study was to investigate how phosphorite helps mitigate the effects of Na/Cl on equipment corrosion during coal pyrolysis. Therefore, molecular dynamics simulations were performed using phosphorite, quartz sand, and austenitic steel, a common material in boilers. Quartz sand (0 0 1) and $Ca_5(PO_4)_3F$ (0 0 1) crystal planes have more moderate and better surface energy and reactivity, which are the most common in the simulations [73–76]. The main components of 316 stainless steel material, a common material for boilers, were used to atomically dope the austenitic steel in the simulation. Considering that the heat exchange surfaces of boilers come into contact with oxygen during industrial operation, the metal on the surface of austenitic steel reacts with oxygen at high temperatures to form an oxide film. Therefore, this research

selected an atomic doping ratio of 55 % Fe, 10 % Cr, 4 % Ni, and 31 % O. Compared with the complex alloy model, the molecular dynamics simulation of a single crystal plane can more clearly analyze the interaction mechanism between Na/Cl and the metal surface, and studies [77,78] have confirmed the effectiveness of this method. The surface energy of FCC metals decreases with the increase of the crystal plane index. The surface energy of the (1 1 0) crystal plane is between the high-index plane, such as (2 1 1), and the low-index plane, such as (1 1 1) [79], which can better reflect the average surface properties of austenitic steel. Therefore, this study selected the austenitic steel (1 1 0) crystal plane for simulation. Therefore, these three surfaces were selected as adsorption matrices for simulation. Adsorption energy (E_{ads}) of ions on the surfaces of these materials was calculated according to **Formula (12)**, where E^*_{ions} represents the total energy of the ions and the material, E^* represents the energy of the individual material, and E_{ions} represents the energy of the individual ion.

$$E_{ads}=E^*_{ions}-E^*-E_{ions} \quad (12)$$

$$D=\frac{1}{6}\cdot\frac{d[r^2(t)]}{dt} \quad (13)$$

The *Forcite* module was used for molecular dynamics simulation. Na/Cl were introduced into the system using the NVT ensemble, with temperatures set at 773.15 K, 873.15 K, 973.15 K, 1073.15 K, and 1173.15 K. The diffusion coefficients of Na^+/Cl^- in the various systems were calculated using the *Mean Square Displacement* (MSD) method, as shown in **Formula (13)**, where $r^2(t)$ is the average square displacement of the particle in time *t*. By determining the adsorption energy of Na/Cl at different sites on the substrate surfaces, the most stable adsorption configurations and the underlying interaction mechanisms were identified. The diffusion coefficients of Na^+/Cl^- provided further insight into how these ions interact with various materials. These results can provide strong mechanistic support for the research on alleviating Na/Cl deposition and corrosion during the thermal utilization of high-sodium and high-chlorine coal.

Results and discussion

Yield of solid and gas pyrolysis products

The char yield and calorific value under different pyrolysis temperatures in the fluidized bed are shown in Fig. 2. To compare the effects of temperature and phosphorite addition on char yield and calorific value, and to minimize experimental costs, this research compared char produced with and without the addition of phosphorite at 15 % of the coal mass. The yields of char produced by pyrolysis of NM and HM at different temperatures and different amounts of phosphorite added are summarized in the Supplementary Material. As in fixed-bed pyrolysis [80,81], with an increase in pyrolysis temperature, the degree of pyrolysis deepens, and the yield of char from both types of coal gradually decreases. From 500 °C to 900 °C, NM char yield decreased from 66.33 % to 51.02 %, while that of HM char yield decreases from 67.84 % to 51.38 %. When phosphorite is added to the coal, the char yield increases at the same pyrolysis temperature compared to pyrolysis without additive in a fluidized bed. When 15 % phosphorite (relative to the coal mass) is added, the char yield of NM increases by 3–10 %, reaching 65.05 % at 700 °C, up from 55.43 %. The effect of phosphorite on HM pyrolysis is smaller, with the char yield increasing by around 3 %. During pyrolysis, Ca can act as a cross-linking agent for the macromolecular structure of coal, fixing some of the macromolecular fragments and increasing the char yield [82,83]. As shown in Fig. 2, the

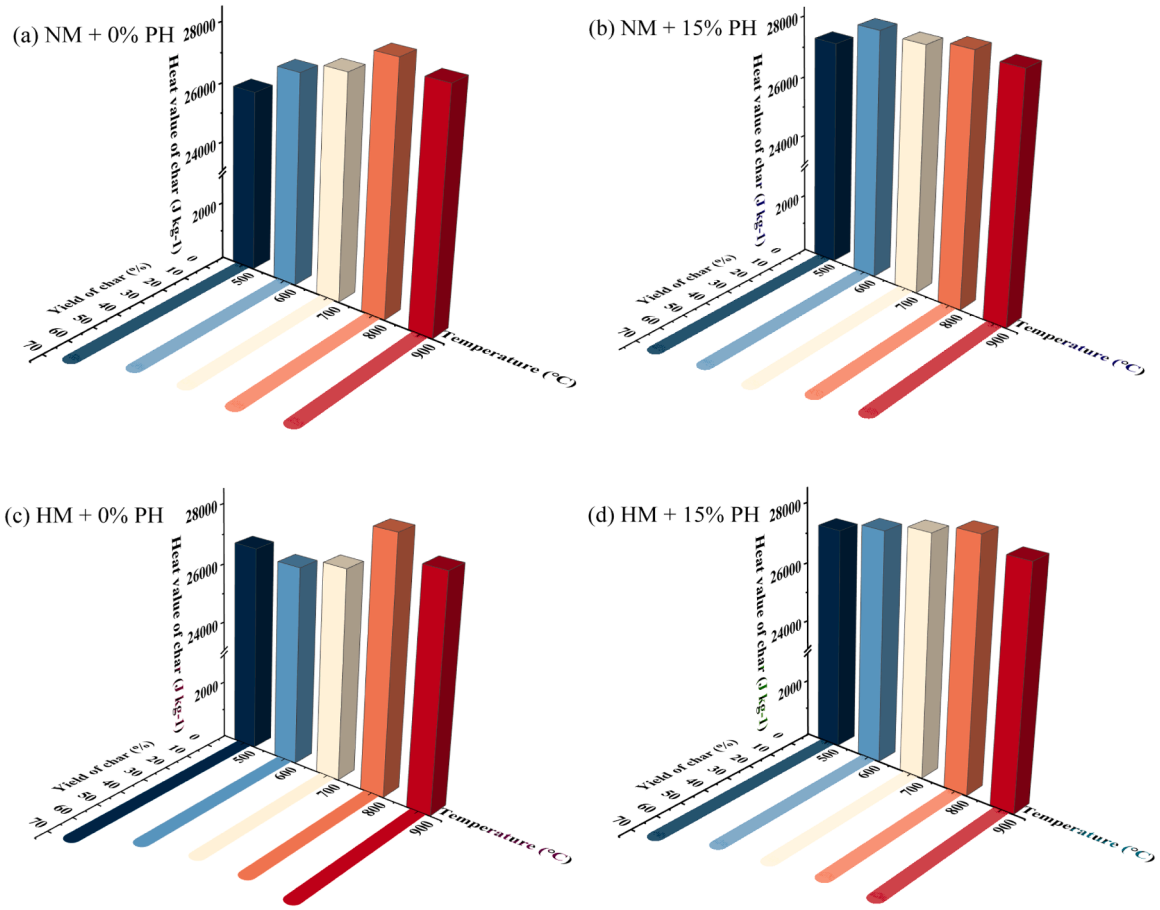

Fig. 2. Yield and heat value of char at different pyrolysis temperatures: (a) NM + 0 % PH, (b) NM + 15 % PH, (c) HM + 0 % PH, (d) HM + 15 % PH.

most significant effect of phosphorite on the char yield is observed between 600 °C and 700 °C, which may be due to the high amount of tar produced in this temperature range. The components of phosphorite, such as CaO and $CaCO_3$, can inhibit the decomposition of macromolecular groups into tar while promoting condensation reactions, reducing tar production and increasing the char yield.

As the temperature increases, calorific value of chars from both NM and HM initially increases and then decreases. Regardless of whether phosphorite is involved in the pyrolysis, both char reaches peak calorific values at 800 °C. Without phosphorite, the calorific values of char at 800 °C are 28299 J kg^{-1} and 28484 J kg^{-1}, respectively. At lower temperatures moisture and volatiles are released while fixed carbon and ash largely remain [84]. Since fixed carbon content strongly correlates with calorific value [85,86], a higher fixed carbon content leads to a higher calorific value. The calorific value of char is also influenced by other factors such as its carbon, hydrogen, oxygen, ash, and moisture content [87]. From Fig. 3, it is observed that below 800 °C, the release of H_2 remains low and stable. However, above 800 °C, a significant amount of hydrocarbons undergo cyclization and aromatization, and organic matter undergoes rapid condensation, leading to large releases of pyrolysis gas and an increase in H_2 release. This increase in H_2 reduces the combustible content of the char and decreases its calorific value. The increase in pyrolysis temperature also leads to higher ash content, which causes some carbon-containing small molecules to remain in the ash [88], further reducing combustion efficiency. As a result, at 900 °C, the calorific values of char from NM and HM decrease to 27936 J kg^{-1} and 27750 J kg^{-1}, respectively. However, after adding phosphorite, the calorific value of the char increases. Calcium-based minerals in phosphorite react with functional groups like carboxyl and hydroxyl to promote condensation reactions, reducing tar and volatile releases and increasing fixed carbon content, thus improving the calorific value. The increase in calorific value is especially prominent in the 500–700 °C temperature range. At 700 °C, the calorific values of char from NM and HM increase by 625 J kg^{-1} and 1074 J kg^{-1}, respectively, after adding 15 % phosphorite (relative to the coal mass).

To compare the quality of pyrolysis gas, we sampled the gas under each operating condition and measured its gas composition. Based on the measurement results, we calculated the cold gas efficiency of the pyrolysis gas under different operating conditions for comparison. As seen in Fig. 3, the generation of pyrolysis gas from NM and HM increases with temperature, regardless of phosphorite addition. At 500 °C, the CO_2 content in NM and HM pyrolysis gases is relatively high, making up 69.42 % and 72.96 % of the total gas, with yields of 518.0 mg g^{-1} and 912.5 mg g^{-1}, respectively. As the pyrolysis temperature increases, the proportion of CO_2 decreases as the yields of other gases increase. By 900 °C, the CO_2 content in NM and HM pyrolysis gas drops to 38.32 % and 37.57 %, respectively. The temperature has a greater impact on CO_2 generation in NM compared to HM. CO_2 is primarily generated by the decomposition of carboxyl groups in coal, which starts around 200 °C and is mostly completed between 500 °C and 600 °C [89]. Therefore, CO_2 production does not change significantly with temperature. The production of CO and CH_4 is more sensitive to temperature. CO is related to the decomposition of phenolic, ether, and carbonyl groups, which break down at approximately 400 °C, 500 °C, and above 700 °C, respectively [90]. CH_4 is primarily produced by the breakdown of alkyl side chains and fatty functional groups in coal, as well as from secondary reactions of char condensation and tar decomposition [91]. As the temperature rises, the production of CO and CH_4 from NM and HM pyrolysis increases rapidly. From 500 °C to 900 °C, the CO and CH_4 yields in HM increase by 646.0 mg g^{-1} and 315.3 mg g^{-1}, respectively, while in NM, the yields increase by 759.8 mg g^{-1} and 352.8 mg g^{-1}. H_2 release is mainly associated with condensation, cyclization and aromatization reactions of coal functional groups. Below 800 °C, H_2 production is minimal in both coals, staying below 100.0 mg g^{-1}. However, at 900 °C, H_2 content and yield increase for both NM and HM. In NM, H_2 content increases from 5.42 % at 800 °C to 6.26 %, with a yield increase from 109.9 mg g^{-1} to 134.3 mg g^{-1}. As for HM, H_2 content increases from 3.74 % to 6.01 %, with a yield increase from 79.8 mg g^{-1} to 153.5 mg g^{-1}.

As shown in Fig. 3, the total volume of pyrolysis gas increases slightly with the increasing addition of phosphorite when co-pyrolyzing with coal. At 700 °C, the total pyrolysis gas yield from NM increases from 1959.0 mg g^{-1} to 2184.4 mg g^{-1}, and from 1574.1 mg g^{-1} to 1705.4 mg g^{-1} for HM. Compared to pyrolysis without additive, adding 9 % phosphorite (relative to the coal mass) leads to a more noticeable change in gas component distribution. However, after adding 15 % phosphorite, the gas composition remains nearly unchanged. In the 500–700 °C temperature range, the effect of phosphorite addition on gas generation is more pronounced, while the influence diminishes significantly when the temperature exceeds 700 °C.

$$\text{R-OH} + CaCO_3 + \text{R'-OH} \rightarrow \text{R-O-Ca-O- R'} + CO_2 + H_2O \quad (R1)$$

$$\text{R-COOH} + CaCO_3 + \text{R'-COOH} \rightarrow \text{R-COO-Ca-COO- R'} + CO_2 + H_2O \quad (R2)$$

The addition of phosphorite influences CO_2 generation in NM and HM pyrolysis, though the effect decreases at higher temperatures. Calcium-containing compounds, such as CaO in phosphorite, catalyze the cracking of tar during pyrolysis [92,93]. In the 500–600 °C range, where tar formation is more significant, these compounds facilitate CO_2 production by cracking tar. Thus, at these temperatures, CO_2 generation increases with higher phosphorite content. Additionally, the generation of H_2 and CH_4 rises with increased phosphorite addition. CaO promotes the dehydrogenation of fatty structures [94] and aids the pyrolysis of aromatic compounds [95], thus generating more H_2. Previous research [96] indicates that calcium compounds can lower the CH_4 generation temperature, promoting its release. On the other hand, CO generation decreases with increasing phosphorite content. This is due to the interaction between Ca in phosphorite and oxygenated functional groups like phenolic, hydroxyl, and carboxyl groups, forming larger macromolecules that release CO_2 and H_2O (as shown in R1 and R2). This consumes some functional groups initially intended for CO generation. Additionally, with higher H_2 and CH_4 release, these gases react with oxygen at higher temperatures, reducing the oxygen content in the gas phase and further inhibiting CO formation. Therefore, phosphorite addition reduces CO production.

For easier comparison, this study summarized the refrigerant gas efficiency under different working conditions in the Supplementary Materials**.** As shown in Fig. 3, the pyrolysis temperature rises, the energy input increases, driving the release of volatiles and the rearrangement of the carbon structure. From 500 °C to 900 °C, the cold gas efficiency for NM and HM increases by 23.04 % and 29.72 %, respectively. Phosphorite addition enhances the pyrolysis of carbon and volatiles, increasing the rate of small gas molecules. At 700 °C, adding 15 % phosphorite increases cold gas efficiency by 2.62 % for NM and 0.77 % for HM.

Combustion performance of char

In this study, char was produced by pyrolyzing two types of coal at varying temperatures and phosphorite concentrations. In order to explore the combustion characteristics, combustion thermogravimetric analysis of char was carried out. The heating program was set to increase the temperature from 30 °C to 1000 °C at a rate of 10 °C min^{-1}, while using standard air (50 mL min^{-1}) to purge the system. The resulting TG-DTG combustion curves of the char are displayed in Fig. 4.

Previous studies [97] have shown that the temperature at which the mass loss rate reaches 50 % during the air-thermogravimetric experiment is referred to as the ignition temperature, $T_{0.5}$ (°C). Using the TG-DTG curves and **Formula (14)**, the reactivity (R) of char was calculated. A higher R value reflects better combustion performance. As shown in Fig. 4, R of the char from NM and HM under various conditions was evaluated. Without phosphorite, R of NM-Char at 500 °C is 0.5736,

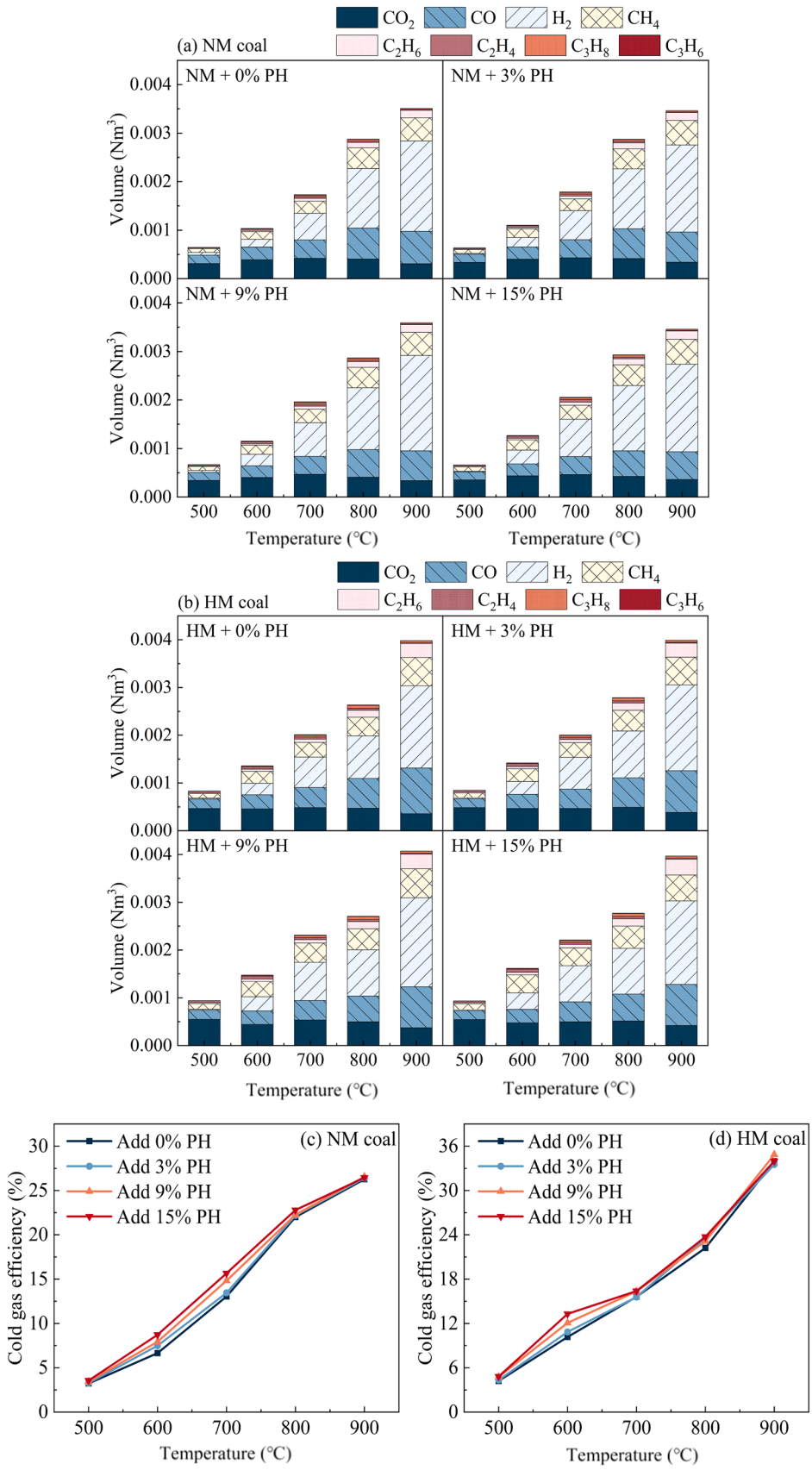

Fig. 3. Gas phase pyrolysis products of NM and HM at different temperatures: (a) Pyrolysis gas components of NM, (b) Pyrolysis gas components of HM, (c) Cold gas efficiency of NM pyrolysis gas, (d) Cold gas efficiency of HM pyrolysis gas.

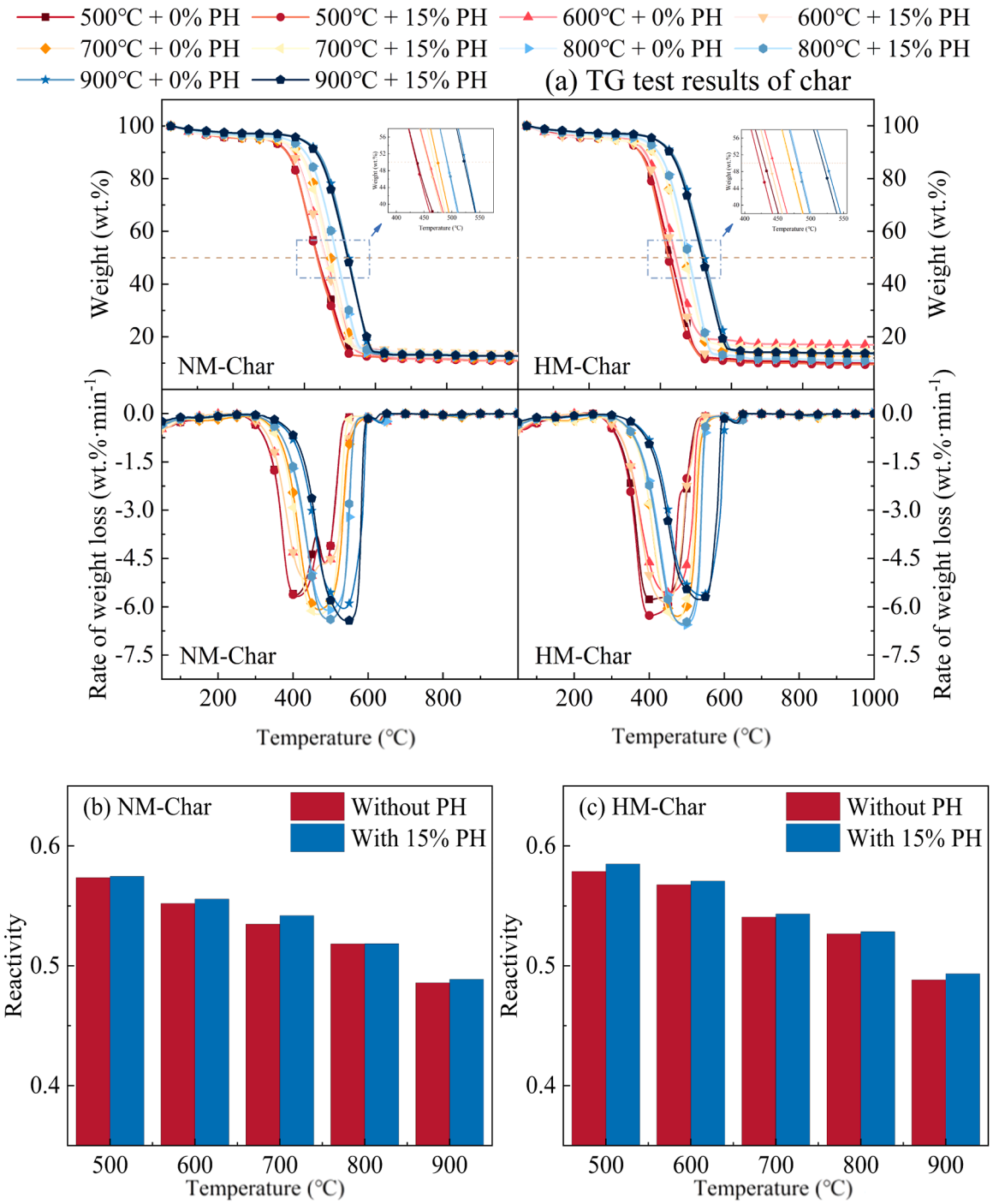

Fig. 4. TG-DTG results and reactivity of char at different pyrolysis temperatures: (a) TG-DTG test curves of char from NM and HM, (b) Reactivity of NM char, (c) Reactivity of HM char.

which decreases to 0.4858 at 900 °C. For HM-Char, R decreased from 0.5787 to 0.4882 under the same conditions. This suggests that char reactivity (R) decreases with increasing pyrolysis temperature, likely because more labile species volatilize, reducing reactive surface sites on the char. Therefore, oxygen adsorption and diffusion on the char surface become more difficult, impeding oxidation reactions.

$$R = \frac{1000 - T_{0.5}}{1000} \tag{14}$$

The addition of phosphorite during coal pyrolysis can slightly improve R of char. At a pyrolysis temperature of 700 °C, R of NM-Char and HM-Char increased by 0.0071 and 0.0026, respectively. This improvement is attributed to the catalytic effect of metal oxides in phosphorite, which promotes specific reactions in the carbon structure of coal, creating additional active sites. The mineral content in phosphorite may also influence the rearrangement of the carbon structure during pyrolysis, making the structure of the char more favorable for interaction with oxygen. However, the overall increase of R due to phosphorite is limited. The effect of phosphorite on R of char varies with different coal types, likely due to variations in coal properties and composition.

By combining the TG-DTG combustion curves of char and the methods described earlier, the combustion characteristic parameters were determined and calculated, as summarized in Table 2, where T

Table 2
Combustion characteristics of char at different pyrolysis temperatures.

Sample	T (°C)	P (%)	T_i (°C)	T_b (°C)	T_{max} (°C)	$(dm/dt)_{max}$ % min^{-1}	$(dm/dt)_{mean}$ % min^{-1}	C (10^{-5})	G (10^{-5})	S (10^{-8})
NM	500	0	332	525	405	−5.663	−0.891	5.137	4.211	8.720
	500	15	331	526	415	−5.701	−0.914	5.204	4.151	9.041
	600	0	346	547	432	−5.183	−0.911	4.330	3.468	7.207
	600	15	342	535	440	−5.134	−0.884	4.389	3.411	7.253
	700	0	371	549	468	−6.116	−0.907	4.443	3.522	7.339
	700	15	366	537	468	−6.269	−0.892	4.680	3.660	7.770
	800	0	381	559	492	−6.137	−0.895	4.228	3.274	6.765
	800	15	381	559	492	−6.420	−0.903	4.422	3.425	7.144
	900	0	408	591	533	−6.079	−0.895	3.652	2.795	5.531
	900	15	415	588	542	−6.473	−0.896	3.758	2.878	5.724
HM	500	0	326	513	403	−5.803	−0.922	5.461	4.417	9.816
	500	15	322	515	405	−6.295	−0.929	6.072	4.827	10.951
	600	0	335	525	456	−5.602	−0.911	4.991	3.667	8.664
	600	15	334	517	440	−5.895	−0.852	5.285	4.011	8.711
	700	0	367	537	473	−6.330	−0.897	4.700	3.647	7.851
	700	15	367	532	473	−6.463	−0.875	4.799	3.723	7.889
	800	0	372	547	495	−6.615	−0.916	4.780	3.592	8.009
	800	15	371	545	488	−6.555	−0.913	4.762	3.620	7.978
	900	0	406	598	536	−5.671	−0.886	3.440	2.606	5.099
	900	15	402	589	533	−5.806	−0.885	3.593	2.710	5.398

represents the pyrolysis temperature and P indicates the mass ratio of phosphorite relative to the coal. With increasing temperature, the reaction initiation temperature of both NM-Char and HM-Char rises significantly. For NM-Char, pyrolyzed at 900 °C, the reaction initiation temperature is 76 °C higher than that at 500 °C, while the maximum weight loss rate increases from −5.663 % min^{-1} to −6.079 % min^{-1}. HM-Char exhibits a similar trend. Both the C and G values of NM-Char and HM-Char decrease as the temperature rises, which suggests that higher temperature makes char combustion less sustainable and degrades its overall combustion performance. This phenomenon is likely due to the increased release of volatile matter during high-temperature pyrolysis, which results in a more stable and compact char structure. Consequently, higher temperatures are required for ignition and complete combustion, leading to reduced reactivity.

In Table 2, it is evident that the reaction start and end temperatures of char do not change significantly upon adding 15 % phosphorite. However, the maximum combustion rates of both chars increase considerably. Calculated C and S indices increased when phosphorite was added, indicating improved combustibility and comprehensive combustion performance. At 500 °C, the C values of NM-Char and HM-

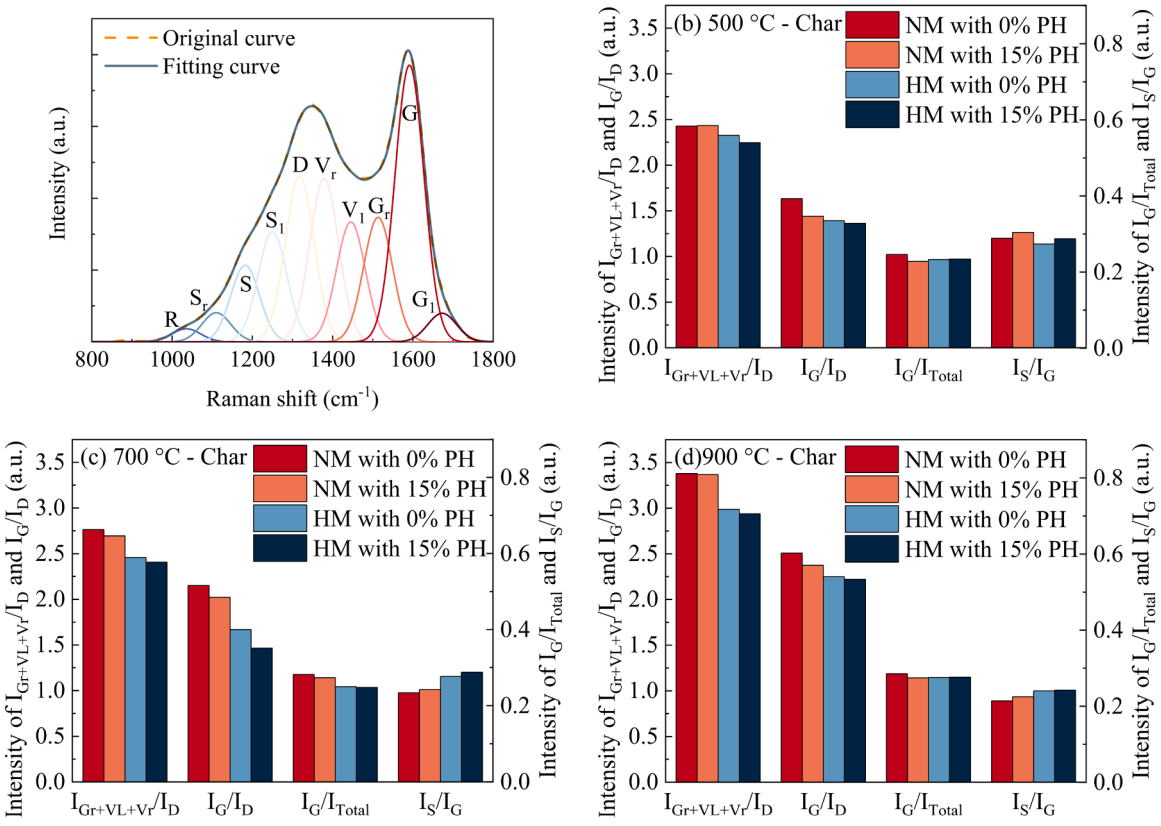

Fig. 5. Raman curve peak fitting example and characteristic parameters of char from NM and HM pyrolysis with different phosphorite addition: Example of the fitted curve for Raman test of char (a) and Raman characteristic parameters of char obtained by pyrolysis at 500 °C (b), 700 °C (c), 900 °C (d).

Char rise by 0.067 and 0.611, respectively, while the *S* values increase by 0.321 and 1.135, respectively. This suggests that phosphorite affects the coal pyrolysis process. Phosphates and metal oxides in phosphorite can alter the char structure and may remain in the final product. These compounds serve as catalysts, accelerating the combustion reaction by lowering activation energy and increasing the oxidation rate [98]. Thus, char produced in the presence of phosphorite shows improved combustion sustainability and performance.

Microstructure of char

Fig. 5 shows the Raman characteristic parameters of char from NM and HM pyrolysis at different temperature. From Fig. 5, it can be observed that as the temperature increases, the $I_{(Gr+VL+Vr)}/I_D$ value of the char increases. This is because higher temperatures promote a deeper pyrolysis reaction, leading to the decomposition of more side chains, low molecular compounds, and oxygen-containing functional groups, which in turn generates more volatiles [99]. Consequently, the defective structures in the char decrease, and the degree of order in the char increases. Similarly, the I_G/I_D ratio also rises with increasing temperature. This increase is attributed to the transformation of defect carbon and amorphous carbon structures into ordered sp^2 hybridized structures [100]. This results in a more ordered char structure and accelerates graphitization. Electron-rich structures, like oxygen-containing functional groups, generally exhibit higher Raman scattering ability, and the total peak area in the Raman spectrum is directly correlated with the quantity of these groups [101,102]. As observed in previous studies [103], higher temperatures reduce the number of oxygen-containing functional groups, thus promoting the formation of volatiles. As a result, the value of I_G/I_{Total} slightly increases with rising temperature. This supports the explanation of the reduced *R* of char with increasing temperature. Additionally, the I_S/I_G ratio decreases as the temperature increases, indicating that high temperatures accelerate the cracking or aromatization of aliphatic structures. This reduces the aliphatic structure in the char and leads to a decrease in the intensity of the S peak. The cracking and aromatization processes facilitate the reaction of C, H, and O, resulting in the generation of more H_2 and CO_2. CO_2 then reacts with the carbon in the char at high temperatures, producing CO. This explains the increased generation of H_2 and CO in the pyrolysis gas with rising temperature.

From Fig. 5, it is evident that the impact of phosphorite on the Raman characteristic parameters of char from NM and HM pyrolysis at various temperatures is similar. Specifically, the values of $I_{Gr+VL+Vr}/I_D$, I_G/I_D, and I_G/I_{Total} decrease when phosphorite is included in the pyrolysis process. Unstable bridge bonds in the coal structure break, resulting in the formation of free radicals. Hydrogen present in the system stabilizes these free radicals, as demonstrated in previous research [104]. With phosphorite present, H_2 production increased, implying that Ca-bearing phases catalyze dehydrogenation and related reactions. This process destabilizes the initially stable free radicals, reducing the ordering in the char structure and increasing defect formation as more unstable bridge bonds break. Consequently, the values of $I_{Gr+VL+Vr}/I_D$ and I_G/I_D decrease. As the degree of graphitization is closely related to the development of active sites and pores, the more developed the pores, the lower the graphitization degree [105]. The addition of phosphorite leads to an increase in CO_2 generation, which attaches to the char surface, promoting crosslinking reactions. These reactions expand micropores and mesopores, while also creating additional active sites on the surface of the char, making it more reactive. This explains the reduction in graphitization and the decrease in the I_G/I_{total} values observed with the addition of phosphorite. Moreover, phosphorite catalyzes the cracking of aromatic structures in the char [106,107], which produces smaller aromatic rings and long-chain aliphatic structures. Long chain aliphatic structures will produce steric groups [108,109] that prevent the condensation of larger aromatic structures, further increasing the I_S/I_G value.

From Fig. 6, it is observed that the interlayer spacing of the carbon (d_{002}) in the char decreases as the pyrolysis temperature increases, whether or not phosphorite is involved in the pyrolysis process. Both coal types exhibit a reduction in the aromatic layer stacking height (L_c) with increasing temperature, while the crystallite size parallel to the aromatic layers (L_a) increases. This behavior is attributed to the release of volatiles during pyrolysis, which reduces impurities within the carbon layers and consequently shortens the interlayer spacing, leading to a more compact char structure. Additionally, higher temperatures promote dehydrogenation and the release of small molecules, which further stabilize the aromatic layer stacking and enhance the overall structural stability of the char, thus lowering L_c. Under elevated temperatures, coal undergoes condensation reactions of aromatic rings, forming larger aromatic structures, which leads to an increase in L_a due to the growth of the aromatic layers.

Furthermore, the inclusion of phosphorite in the pyrolysis process significantly influences the microcrystalline structure of the char. Phosphorite-derived phosphate species can form C–O–P/C–P linkages, hindering dense graphitic stacking and promoting more cross-linked char structures. Moreover, the calcium and magnesium present in the phosphorite catalyze reactions between the volatiles and carbon structure, forming stable compounds or complex salts at high temperatures. These products remain in the char, obstructing the approach of the carbon layers. Therefore, the d_{002} value is higher in chars produced with phosphorite. The cross-linking introduced by phosphorite may vertically connect the aromatic layers, guiding their growth and promoting their directed stacking along their surfaces. This increases the stacking units, leading to an increase in L_c. However, the adsorption of phosphate salts and minerals around the carbon layers, as well as their interaction with surface free radicals, reduces the lateral extension of the aromatic layers and leads to a decrease in L_a.

From Fig. 7, it can be observed that the impact of temperature on the pore characteristics of chars from NM and HM is consistent. As the temperature increases, the pyrolysis reaction intensifies, leading to the decomposition of organic matter and the release of small volatile molecules. This results in the formation of more pores on the char surface, as well as the connection of existing pores. Consequently, the specific surface area of the char increases with higher temperatures. Increased surface area promotes volatile release; subsequent cracking at higher temperatures further expands pore volume. Meanwhile, the average pore diameter decreases, likely due to the formation of more micropores and mesopores during the cracking process. As discussed in the Raman analysis, the char structure becomes more ordered at higher temperatures, with closer carbon atom arrangements. This reduces the size and number of larger or irregular pores, creating a more uniform pore structure. While the specific surface area and total pore volume increase, the proportion of small pores increases, leading to a decrease in the average pore diameter.

The involvement of phosphorite in pyrolysis results in a significant change in the pore structure of the char compared to when phosphorite is absent. Phosphorite contributes to more complex interactions between the organic matter and mineral components during pyrolysis. The calcium- and phosphorus-containing compounds in phosphorite promote cracking reactions, especially at high temperatures, generating more micropores and mesopores. This increases both the specific surface area and the total pore volume of the char. Furthermore, phosphorite exhibits catalytic effects on pyrolysis under high temperatures, potentially expanding or connecting the mesopores and micropores, thereby forming larger macropores. Phosphate salts can also react with other minerals in the coal, producing stable silicate and complex salt compounds. These metal oxides and complex salts may form strong chemical bonds with the carbon atoms in the coal, enhancing the stability of larger pores and reducing the shrinkage of pores. As a result, the average pore diameter of the char increases when phosphorite is added.

Combined with the BET analysis results, SEM figures clearly reveal the modulating effect of phosphorite on the porous structure of char, as

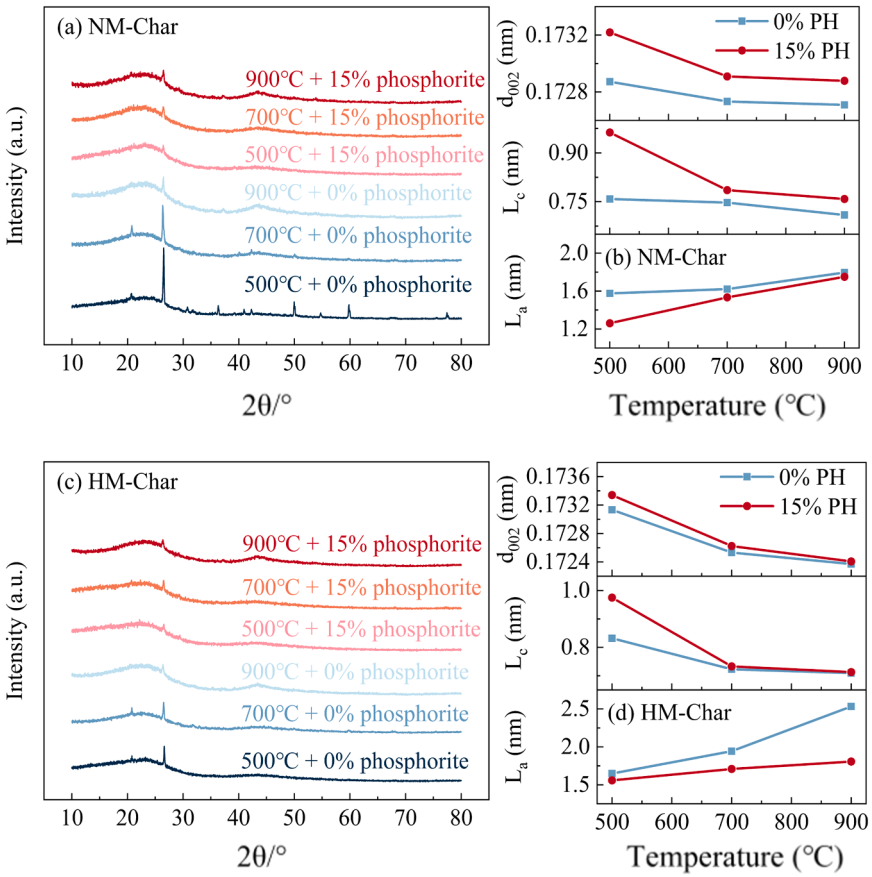

Fig. 6. Microscopic characterization analysis of char under different pyrolysis conditions: (a) XRD patterns of NM char, (b) Carbon microcrystalline parameters of NM char, (c) XRD patterns of HM char, (d) Carbon microcrystalline parameters of HM char.

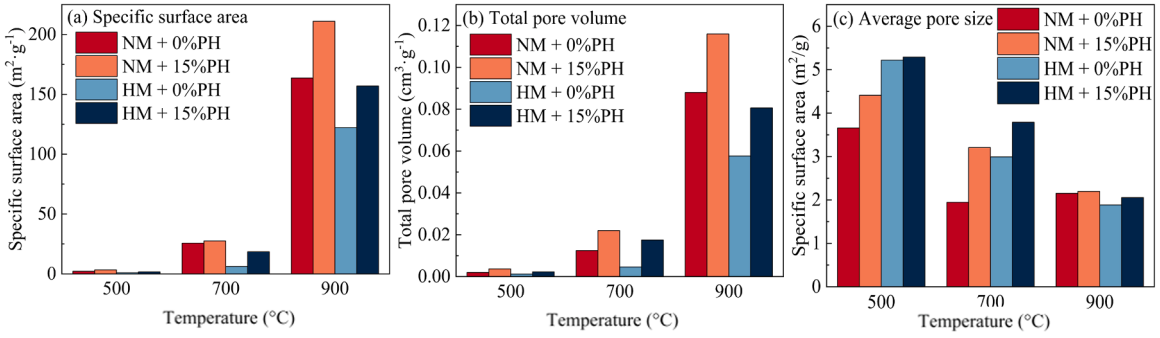

Fig. 7. BET analysis of char from NM and HM under different pyrolysis conditions: (a) Specific surface area, (b) Total pore volume, (c) Average pore size.

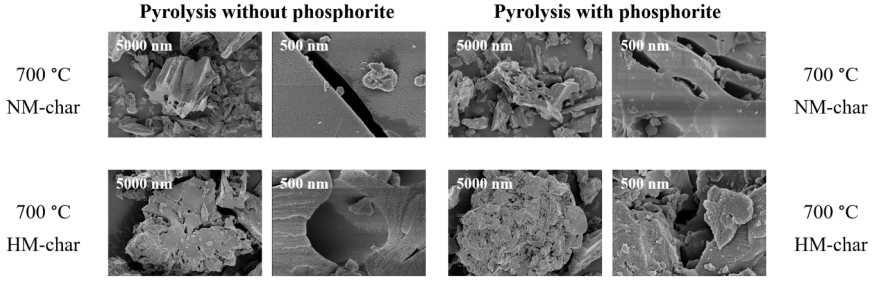

Fig. 8. Scanning electron microscope figures of char produced during coal pyrolysis with and without phosphorite.

shown in Fig. 8. For char produced by pyrolysis of NM, without the addition of phosphorite, the char surface is relatively smooth, with sparse micropores. The addition of phosphorite significantly improves the surface roughness of the char, increases the number of pores, and forms a large number of well-connected pores, directly confirming the BET conclusion of increased specific surface area and total pore volume. The same pattern is observed for char produced by pyrolysis of NM. In the absence of phosphorite, although localized pores are visible in the char, the pores are dispersed. With the addition of phosphorite, the char exhibits a fluffy, porous morphology with nested macropores and secondary micropores, directly reflecting the increase in average pore size as measured by BET. Scanning electron microscopy figures reveal that the changes in the char micromorphology are consistent with the findings from the BET analysis.

Effect of phosphorite on the release of Na/Cl

Chemical reaction

Simulations and experiments examining the reaction pathways and chemical mechanisms of Na/Cl during co-pyrolysis have confirmed that phosphorite inhibits Na/Cl release through three mechanisms: chemical reactions, selective adsorption, and solid retention. Regarding chemical reactions, the reaction process of Na/Cl with other components are complex during coal pyrolysis. Water-soluble Na/Cl reacts with Ca, Si, and P components during pyrolysis to form high-melting-point $CaCl_2$, Na_2CaSiO_4, Na_3PO_4, and $Na_3Mg(CO_3)_2Cl$. These compounds are more stable at high temperatures, thus preventing Na/Cl volatilization. To determine the specific inhibitory effect of phosphorite on Na/Cl release, this experiment investigated the amount of Na/Cl released under different operating conditions. As shown in Fig. 9, phosphorite significantly influences the release of Na/Cl during the pyrolysis process. Measured Na/Cl release ratios indicate particularly high Cl volatilization, with NM and HM releasing 60.43 % and 65.18 %, respectively, at 500 °C. Conversely, the release of Na is lower at 500 °C, but increases at higher temperatures. At 900 °C, NM and HM release 31.14 % and 24.74 % of Na, respectively. When phosphorite is added, the release of Na/Cl decreases, with a more pronounced reduction as temperature increases. After adding 15 % phosphorite, the release of Na decreases by 6.04 % and 5.59 % at 500 °C, and 15.66 % and 11.17 % at 900 °C for NM and HM, respectively. The release of Cl is more significantly affected by phosphorite, with a 16.05 % and 17.66 % decrease at 900 °C for NM and HM, respectively.

This is because phosphorite introduces oxides such as SiO_2, CaO, and MgO, which react with Na/Cl during pyrolysis to form stable chlorine-sodium-metal-oxygen and silicon-sodium-metal-oxygen compounds [98,110–112]. The calcium phosphate and fluorophosphate can also combine with Na/Cl to form phosphate-metal-sodium compounds, which reduces the gaseous release of Na/Cl during pyrolysis. The chemical reaction equations for these processes are shown in R(3)-(12).

$$Ca_3(PO_4)_2 + 6NaCl \rightarrow 3CaCl_2 + 2Na_3PO_4 \quad (R3)$$

$$MgO + 3NaCl + 2CO_2 + H_2O \rightarrow Na_3Mg(CO_3)_2Cl + 2HCl \quad (R4)$$

$$2HCl + MgO \rightarrow MgCl_2 + H_2O \quad (R5)$$

$$4NaCl + 2Al_2O_3 + 5SiO_2 \rightarrow 4NaAlSiO_4 + SiCl_4 \quad (R6)$$

$$8NaCl + 4CaO + 8SiO_2 \rightarrow 2Na_4Ca_2Si_3O_{10} + 2SiCl_4 \quad (R7)$$

$$SiCl_4 + 3H_2O \rightarrow 4HCl + H_2SiO_3 \quad (R8)$$

$$H_2SiO_3 + CaO \rightarrow CaSiO_3 + H_2O \quad (R9)$$

$$14NaCl + 8Ca_3(PO_4)_2 + 8SiO_2 \rightarrow 2Na_7Ca_{4.5}(P_2O_7)_4 + 7CaCl_2 + 8CaSiO_3 \quad (R10)$$

$$2Ca_5(PO_4)_3F + 18NaCl \rightarrow 9CaCl_2 + 6Na_3PO_4 + CaF_2 \quad (R11)$$

$$2Ca_5(PO_4)_3F + 9Na_2SO_4 \rightarrow 9CaSO_4 + 6Na_3PO_4 + CaF_2 \quad (R12)$$

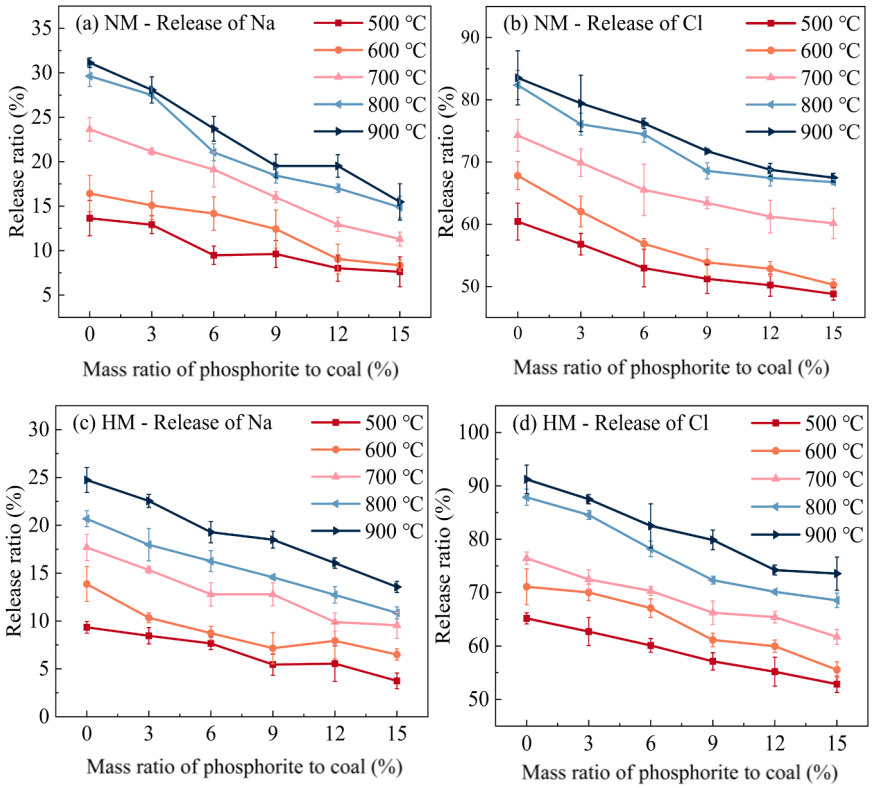

Fig. 9. Effect of phosphorite on the release of Na and Cl during pyrolysis: (a) Effect of Na release during NM pyrolysis, (b) Effect of Cl release during NM pyrolysis, (c) Effect of Na release during HM pyrolysis, (d) Effect of Cl release during HM pyrolysis.

Selective adsorption

To investigate the effect of phosphorite on Na/Cl release, this study uses quartz sand and austenitic steel as references to better assess the capture effect of phosphorite. Molecular dynamics simulations were performed to analyze the adsorption configurations and binding energies of Na/Cl on different materials, and to calculate their corresponding diffusion coefficients. The adsorption configuration optimization and adsorption energy calculation results of molecular dynamics simulation are presented in the Supplementary Material. The simulation results show that the adsorption energies for both Na and Cl are negative, indicating that the adsorption process is exothermic and spontaneous, leading to a more stable system. Phosphorite shows the highest adsorption energy for Na at the O site (-2.0101 eV) and the lowest for Cl at the P site (-2.3736 eV). This suggests that Na and Cl have more stable adsorption configurations at the O and P sites, respectively. Compared to quartz sand, austenitic steel, and phosphorite, the absolute value of adsorption energy of quartz sand and Na/Cl adsorption configuration is the lowest, followed by austenitic steel. Na and Cl have the most stable adsorption on the surface of phosphorite. This phenomenon can explain that compared with quartz sand, Na/Cl is more easily adsorbed on the surface of austenitic steel. Therefore, during the thermal utilization of NM and HM, Na/Cl will be more deposited on the surface of the heat exchanger. Quartz sand, a heat carrier, has a weak adsorption effect on Na/Cl. Large amounts of Na/Cl deposits can affect the heat transfer efficiency of the heat exchange surface and cause corrosion. It is necessary to introduce phosphorite, which is more adsorbent of Na/Cl, to reduce the impact of Na/Cl on the heat exchange surface. Phosphorite can better capture Na/Cl, prevent it from being deposited in large quantities on the surface of austenitic steel, alleviate the negative impact of corrosion, and thus improve the safety and economy of equipment operation.

Solids retention

Fig. 10 presents the diffusion coefficients of Na^+/Cl^- across different systems. A higher diffusion coefficient indicates that the ions have a stronger ability to diffuse within the system, making their movement or migration easier. The diffusion coefficients increase with temperature, suggesting that higher temperatures facilitate the diffusion of Na^+/Cl^- in all three systems. The diffusion coefficients of Na^+/Cl^- in austenitic steel are the highest, indicating that the austenitic steel system likely has a more open structure, which enhances the movement of these ions and allows them to diffuse at the fastest rate. This greater diffusivity can lead to ions migrating more easily to the heated surface of equipment, thereby affecting normal operations. In contrast, the diffusion coefficients in the phosphorite system are the lowest, indicating that Na^+/Cl^- are more strongly confined near the adsorption sites. This results in more difficulty for them to migrate and requires overcoming higher energy barriers to diffuse.

In conclusion, the mechanism by which phosphorite reduces Na/Cl release ratios is that it captures and reacts with Na/Cl. The combined effects of higher adsorption energy and lower diffusion coefficients can immobilize the Na/Cl released by coal pyrolysis on the surface, allowing it to participate more in the reaction and produce more stable compounds. This process can significantly reduce the amount of Na/Cl released, making it more difficult for Na/Cl to be captured by the heat exchange surfaces in the boiler. Molecular dynamics analysis results support the idea that adding phosphorite to coal pyrolysis is an effective way to immobilize Na/Cl, reducing the release of corrosive substances, minimizing their impact on equipment, and improving the clean utilization efficiency and value of low-rank coal resources.

Follow-up work plan

In future research, we will consider designing a device to study Na/Cl deposition corrosion at the tail end of a fluidized bed reactor. This device will simulate the actual high-sodium coal pyrolysis and combustion process inside an industrial boiler, thereby studying the effects of Na/Cl on the tail end heating surface under different reaction conditions. Based on the experimental results, we will analyze the Na/Cl deposition and corrosion characteristics and assess the role of phosphorite.

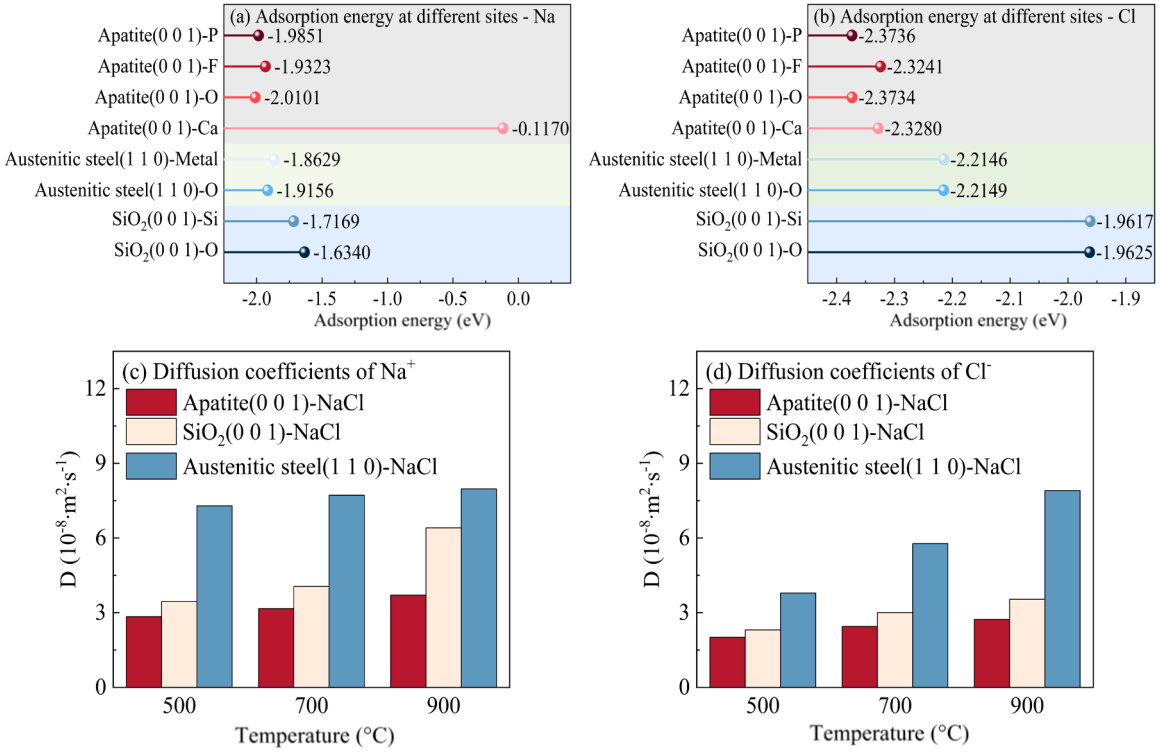

Fig. 10. Molecular dynamics simulation results: Adsorption energy at different sites – Na (a) / Cl (b) and diffusion coefficient of Na^+ (c) / Cl^- (d) on different substances.

Reducibility of phosphorite after co-pyrolysis

The conversion ratio can be obtained by reducing the untreated and the co-pyrolyzed phosphorite in a fixed bed reactor respectively. Based on prior research [54,113], the carbon reduction of phosphorite is generally described by a first-order reaction model. The corresponding kinetic equation for first-order reactions is shown in **Formula (15)**. Using the Arrhenius equation, **Formula (16)** and **Formula (17)** can be derived. In these formulas, w_0 represents the mass fraction of P_2O_5 in the raw material (%), A (min^{-1}) is the pre-exponential factor, E_a (kJ mol^{-1}) is the activation energy, R (kJ mol^{-1} K^{-1}) is the molar gas constant, and T (K) is the temperature. The relationship between $\ln[1/(1-\alpha)]$ and time was calculated, and the slope of the conversion ratio curve at different temperatures was used to determine the reaction rate constant k (min^{-1}). The fitting results are shown in Table 3, with the correlation coefficient (r^2). Based on these data, a plot of $\ln k$ and $1/T$ was constructed. As shown in **Formula (17)**, the slope of this curve corresponds to $-E/R$. The fitting results of $\ln k$ and $1/T$ are shown in Table 4. The activation energy of the reaction can be calculated from these results. The above data and calculation results are shown in Fig. 11.

$$\frac{d\alpha}{dt} = k(w_0 - \alpha) \tag{15}$$

$$k = A \cdot \exp\left(-\frac{E}{RT}\right) \tag{16}$$

$$\ln k = \ln A - \frac{E}{RT} \tag{17}$$

Fig. 11 demonstrates that the conversion ratio of phosphorite increases with higher temperatures, and continues to rise as the reaction time progresses. This suggests that elevated temperatures provide the necessary energy for the reduction reaction. When untreated phosphorite undergoes reduction at 1250 °C for 80 min, its conversion ratio reaches 40.95 %. In contrast, phosphorite recovered after co-pyrolysis with NM achieves a conversion ratio of 60.39 % under the same conditions. Phosphorite recovered from co-pyrolysis with HM reaches a conversion ratio of 58.29 %. The pretreatment process can effectively improve the conversion ratio of phosphorite [114]. These results indicate that co-pyrolysis with coal serves as a pre-treatment for phosphorite, effectively enhancing its conversion ratio. The oxide components from coal, such as MgO, CaO, and SiO_2, attach to the surface of phosphorite. During high-temperature reduction, these components alter the reaction pathways, improve material flowability, and enhance heat and mass transfer [115,116], all of which contribute to an increased conversion ratio of phosphorite. Furthermore, both NM and HM contain compounds such as NaCl and $NaSO_4$, which can react with $Ca_5(PO_4)_3F$, the main component of phosphorite. The resulting products, $Ca_3(PO_4)_2$ and Na_3PO_4, are more easily reduced by coal than $Ca_5(PO_4)_3F$, leading to an improved conversion ratio of the recycled phosphorite. The reaction pathways for these processes are shown in R(11)-R(12) and R (13)-(19).

Table 3
Reaction rate constant k and r^2 at different temperatures.

Temperature (°C)	Reduction of untreated phosphorite		Reduction of phosphorite pyrolyzed with NM		Reduction of phosphorite pyrolyzed with HM	
	k (min^{-1})	r^2	k (min^{-1})	r^2	k (min^{-1})	r^2
1150	0.00257	0.941	0.00531	0.982	0.00488	0.972
1200	0.00353	0.966	0.00689	0.965	0.00653	0.971
1250	0.00495	0.915	0.00858	0.956	0.00819	0.990

Table 4
The fitting results under different systems.

System	$\ln k$ (min^{-1})	E (kJ mol^{-1})	r^2
Reduction of untreated phosphorite	$\ln k = -14195.26/T + 4.00$	118.02	0.997
Reduction of phosphorite pyrolyzed with NM	$\ln k = -10405.36/T + 2.08$	86.51	0.998
Reduction of phosphorite pyrolyzed with HM	$\ln k = -11232.80/T + 2.58$	93.39	0.995

$$2Ca_5(PO_4)_3F + 15\,C \rightarrow 3\,P_2(g) + 15CO(g) + 9CaO + CaF_2 \tag{R13}$$

$$CaO + SiO_2 \rightarrow CaSiO_3 \tag{R14}$$

$$2MgO + SiO_2 \rightarrow Mg_2SiO_4 \tag{R15}$$

$$2CaO + MgO + 2SiO_2 \rightarrow 2CaO{\bullet}MgO{\bullet}2SiO_2 \tag{R16}$$

$$4Ca_5(PO_4)_3F + 3SiO_2 \rightarrow 6Ca_3(PO_4)_2 + SiF_4 + 2CaSiO_3 \tag{R17}$$

$$Ca_3(PO_4)_2 + 5\,C + 3SiO_2 \rightarrow P_2(g) + 5\,CO(g) + 3CaSiO_3 \tag{R18}$$

$$2Na_3PO_4 + 5C + 3SiO_2 \rightarrow P_2(g) + 5CO(g) + 3Na_2SiO_3 \tag{R19}$$

Kinetic analysis shows that at 1150 °C, the reduction reaction rate constant k for untreated phosphorite is 0.00257 min^{-1}, which increases to 0.00495 min^{-1} at 1250 °C. This demonstrates that temperature increases promote the reduction reaction. At 1150 °C, the k value for phosphorite recovered after co-pyrolysis with NM is 0.00531 min^{-1}, while for HM it is 0.00488 min^{-1}, which are 2.07 and 1.90 times higher than that for untreated phosphorite. At 1200 °C, the ratio of $k_{\text{(Co-pyrolyzed phosphorite)}}$ / $k_{\text{(Untreated phosphorite)}}$ for NM and HM are 1.95 and 1.85, respectively, and at 1250 °C, they are 1.73 and 1.65. This indicates that co-pyrolysis consistently results in a higher reaction rate constant for phosphorite at all temperatures. The effect of co-pyrolysis is more pronounced at lower reduction temperatures. The activation energies for the reduction reactions were also calculated, $E_{\text{(Phosphorite pyrolyzed with NM)}} < E_{\text{(Phosphorite pyrolyzed with HM)}} < E_{\text{(Untreated phosphorite)}}$. The activation energy for untreated phosphorite is 118.02 kJ mol^{-1}, while for phosphorite co-pyrolyzed with NM and HM, the values are 86.51 kJ mol^{-1} and 93.39 kJ mol^{-1}, respectively. This confirms that co-pyrolysis with coal significantly reduces the activation energy, increases the reaction rate, and accelerates the reaction, thus enhancing phosphorite utilization and energy efficiency. The mechanism diagram for the effect of co-pyrolysis with low-rank coal and phosphorite on gas-solid products is shown in Fig. 12.

Process flow and economic analysis

At present, there have been studies on the use of phosphate as an additive in biomass utilization, and studies on calcium-based additives in coal pyrolysis. However, there has been no systematic study on the application of natural phosphorite to high-sodium low-rank coal pyrolysis system to achieve the improvement of char/gas product performance and the inhibition of Na/Cl release. Moreover, most studies only focus on experimental conditions and feasibility, and few studies propose suitable technical routes for the use of this type of additive. Therefore, this study is not only innovative in terms of experimental exploration and mechanism exploration, but also designs a coal-phosphorite co-pyrolysis coupling process technology route.

The technology pathway proposed in this study is illustrated in Fig. 13. Following the co-pyrolysis of high-sodium low-rank coal and phosphorite, the pyrolysis gas can be directly captured as a chemical raw material or fuel. After separating char from the slag, the phosphorite is fed into a high-temperature reduction furnace, where it undergoes carbothermal reduction with char or coal to produce yellow phosphorus. When yellow phosphorus is converted into phosphoric acid in the hydration absorption tower, the product can be directly used in the

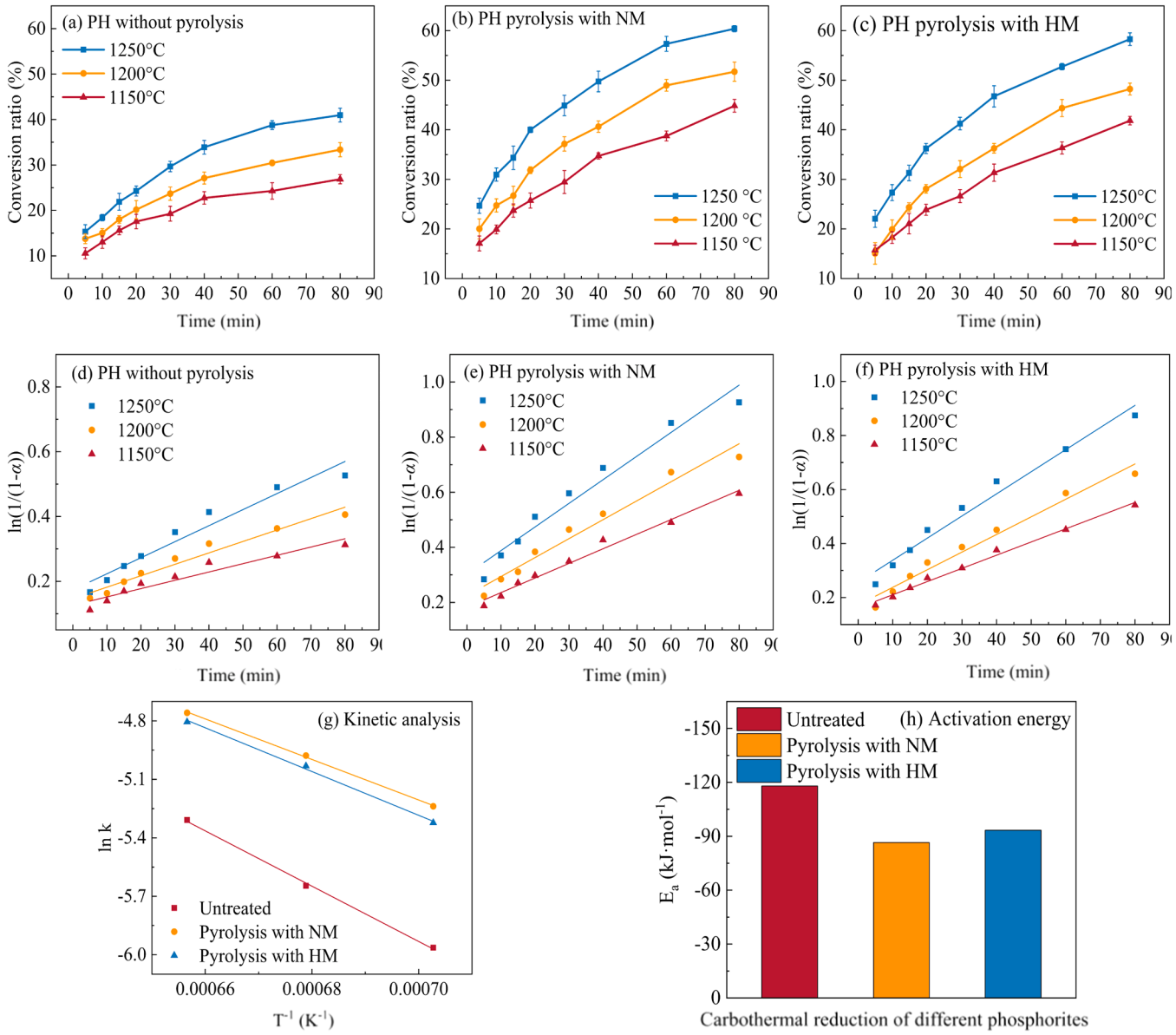

Fig. 11. Conversion ratio of phosphorite under different reaction times and kinetic analysis of carbothermal reaction: (a) Conversion ratio of phosphorite without co-pyrolyzed, (b) Conversion ratio of phosphorite co-pyrolyzed with NM, (c) Conversion ratio of phosphorite co-pyrolyzed with HM, (d) ln(1/(1-α))-t of phosphorite co-pyrolyzed without co-pyrolyzed, (e) ln(1/(1-α))-t of phosphorite co-pyrolyzed with NM, (f) ln(1/(1-α))-t of phosphorite co-pyrolyzed with HM, (g) Kinetic analysis of different phosphorite, (h) Activation energy of different phosphorite.

production of phosphorus chemical products. Additionally, the separated char can find applications in metallurgy, power generation, chemical engineering, and other industrial processes.

The process developed in this study enhances the utilization of high-sodium coal by improving the quality of pyrolysis products and mitigating Na and Cl emissions, thereby increasing product value, extending equipment maintenance intervals, and lowering operational costs. For the phosphorite utilization, this process delivers superior economic performance compared to conventional thermal and wet phosphoric-acid processes. As shown in Table 5, the proposed route yields high-purity products with elevated conversion ratios, enables resource recycling, and thus achieves greater overall cost-effectiveness.

Recently, various additives have been explored to enhance char yield, and boost the cold-gas efficiency during pyrolysis of low-rank, high-sodium coal, as shown in Table 6. Adding a small amount of additives can improve the quality of coal pyrolysis products. In order to evaluate the industrial application potential of the coal-phosphorite synergistic pyrolysis system, low-grade phosphorite and common high-purity calcium-based additives are compared in key economic and engineering indicators, as shown in Table 7. The natural particle form of phosphorite is suitable for fluidized bed and similar large-scale devices without additional pretreatment. The existing conventional fluidized bed can also be directly used for coal pyrolysis and phosphorite reduction without the need for new construction or modification. The price of phosphorite is only 1/5–1/10 of that of conventional pure calcium additives, and China has abundant reserves of medium and low-grade phosphorite, which can be supplied in batches at low cost. The pyrolyzed slag of phosphorite is used as a raw material for thermal reduction. Therefore, this technology has good resource coupling and recycling potential, can improve the conversion ratio of phosphorite, and obtain higher economic benefits. In summary, the process proposed in this study has good prospects for industrial scale-up.

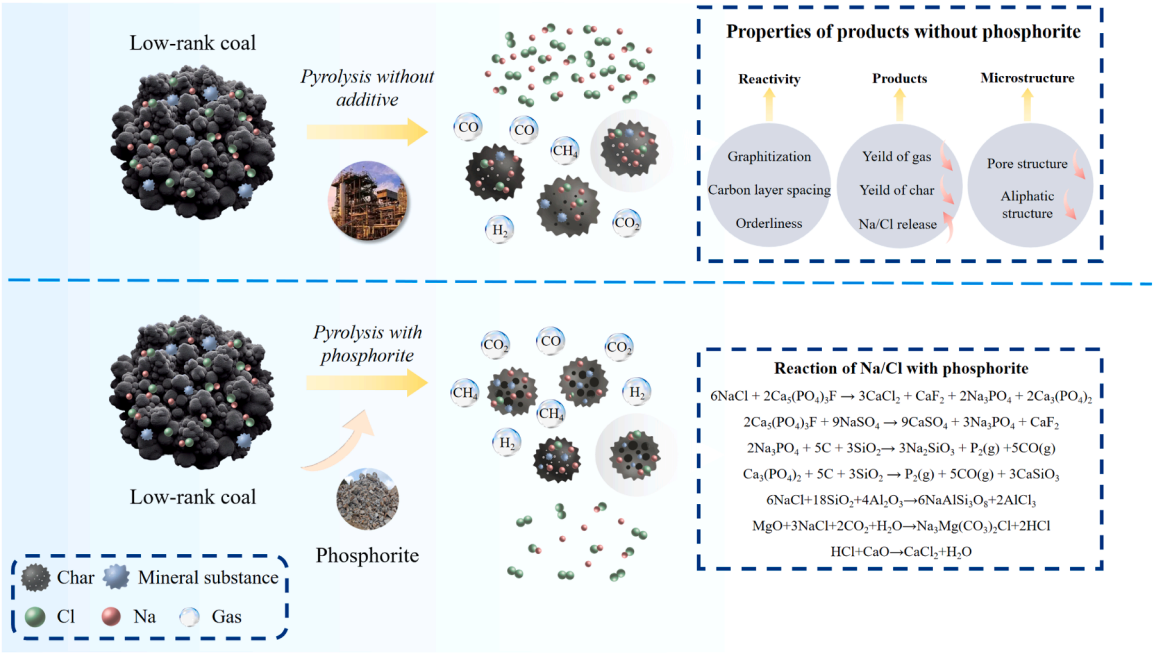

Fig. 12. Mechanism diagram of the effect of co-pyrolysis of low-rank coal mixed with phosphorite on solid-gas products.

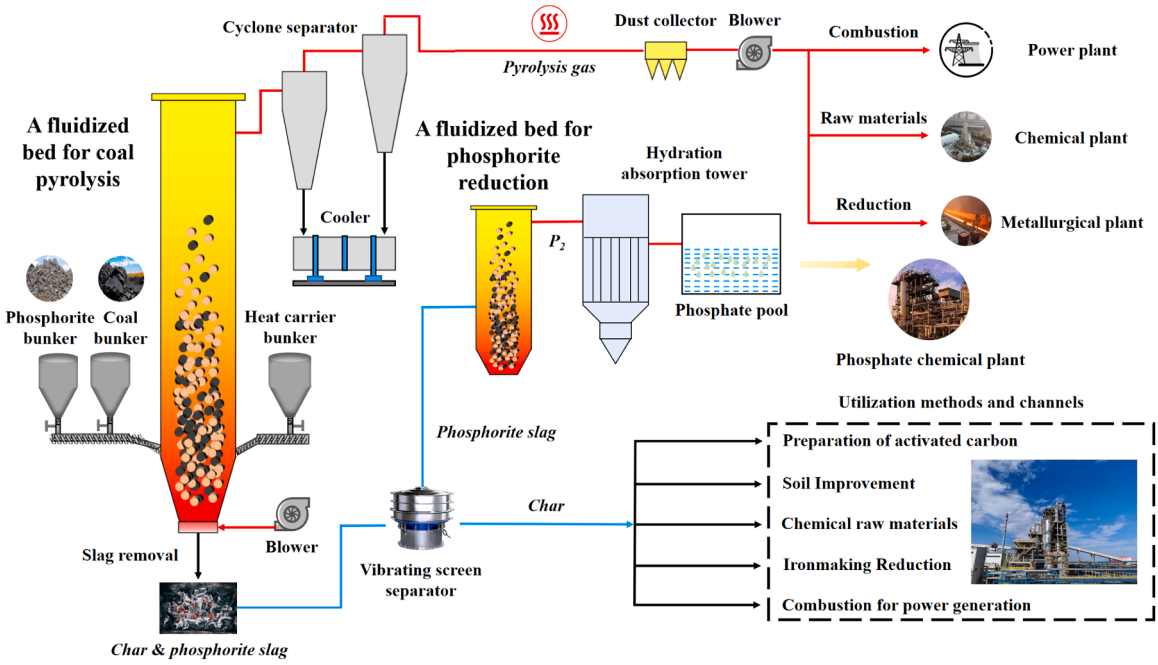

Fig. 13. Technical route of coal-phosphorite synergistic pyrolysis system.

Conclusion

This study experimentally explored the coupled pyrolysis-carbothermal reduction technology of high-sodium, low-rank coal and low-grade phosphorite, and analyzed the influencing mechanisms. By analyzing its economic and feasibility, this study primarily provides innovative technical routes and theoretical foundations for the clean utilization of high-sodium, low-rank coal and the resource utilization of phosphorite. Specific research conclusions are as follows.

1. The addition of phosphorite increased the yield of char produced from the pyrolysis of high-sodium, low-rank coal, and the calorific value of the char also increased accordingly. The cold gas efficiency of the pyrolysis gas increased with increasing phosphorite addition.
2. The addition of phosphorite significantly reduced the Na/Cl release ratio during the pyrolysis of high-sodium, low-rank coal. The greater the amount of phosphorite added, the lower the Na/Cl release under the same operating conditions.
3. Raman and XRD characterization revealed that phosphorite can increase micropores and active sites through Ca-O-C and C-P bond crosslinking, reducing the degree of graphitization and promoting the reactivity of the char.
4. Molecular dynamics calculations show that the adsorption capacity of Na/Cl on phosphorite surfaces is significantly stronger than that

Table 5
Comparison of different technical routes for phosphorite reduction [117–120].

Process for preparing phosphoric acid	Wet reduction	Carbothermal reduction	Co-pyrolysis reduction
Conversion ratio	> 80 %	30–50 %	40–60 %
Product purity	20–40 %	50–60 %	50–60 %
By-products	$CaSO_4 \cdot 2\ H_2O$	Slag rich in CaO and SiO_2	Slag rich in CaO and SiO_2
By-product treatment	Requires higher cost processing	Used as auxiliary cementitious material for cement and concrete	Used as auxiliary gelling material or fluidized bed heat carrier
Economic evaluation	High plant construction cost, low energy consumption, high post-processing cost	Low plant construction cost, high energy consumption, low post-processing cost	Low plant construction cost, moderate energy consumption, slag can be recycled as fluidized bed heat carrier

Table 6
Previous studies on the effects of calcium-based additives on the pyrolysis process[121–124].

References	Ban et al.	Shang et al.	Cheng et al.	Li et al.
Additive	$Ca(OH)_2$	Bauxite residue	Fe_2O_3/CaO	$CaCl_2$
Additive ratio	5 %	10 %–20 %	7 wt%	10 wt%
Char yield	Reduction	Exaltation	Exaltation	Exaltation
Tar yield	Reduction	Reduction	-	-
Gas yield	Exaltation	Exaltation	Exaltation	Exaltation
Cold gas efficiency	Exaltation	Exaltation	Exaltation	Exaltation

Table 7
Comparison between phosphorite and traditional calcium-based additives.

Index	Phosphorite	Calcium-based additives
Price(¥/t)	200–300	1200–2500
Resource reserves	Extremely rich	Relying on industrial synthesis, resources are relatively limited
Potential for recycling by-products	Pyrolysis residue can be directly used in thermal phosphoric acid production	Difficulty in recycling
Engineering adaptability	Directly used in conventional reactors such as fluidized beds without pretreatment	Granulation or dispersion is required, which increases the complexity of the process
Cost controllability	Low	High
Industry amplification maturity	Coupling with the existing phosphorus chemical industry and coal pyrolysis industry chain	Mainly limited to laboratory or pilot scale

on quartz sand and austenitic steel. Molecular dynamics simulations reveal that the Na/Cl diffusion coefficient is lowest in the phosphorite system, which corroborates the experimental findings.

5. This study designed a new process for the co-pyrolysis of coal and phosphorite. Phosphorite is low-cost, and the recovery of pyrolysis slag for carbothermal reduction to produce yellow phosphorus effectively improves its conversion ratio. This process achieves low-cost production and resource recycling, offering excellent economic value.

Funding

Thanks for the financial support by the Fundamental Research Funds for the Central Universities (2022ZFJH004).

CRediT authorship contribution statement

Ruiqing Jia: Writing – review & editing. **Yingchi Chen:** Software, Methodology. **Dong Ma:** Writing – review & editing. **Yufei Liu:** Formal analysis. **Bin Zhang:** Writing – review & editing, Writing – original draft. **Zhihua Tian:** Writing – original draft, Methodology. **Qinhui Wang:** Writing – review & editing, Project administration. **Ying Zhao:** Writing – review & editing, Formal analysis.

Declaration of Competing Interest

The authors declare that they have no known competing financial interests or personal relationships that could have appeared to influence the work reported in this paper.

Acknowledgments

Thanks for the technical and financial support of Dongfang Electric Corporation-Zhejiang University Joint Innovation Research Institute. Thanks for the financial support by the Fundamental Research Funds for the Central Universities (2022ZFJH004).

Appendix A. Supporting information

Supplementary data associated with this article can be found in the online version at doi:10.1016/j.jece.2025.118929.

Data availability

Data will be made available on request.

References

[1] D.M. Madhuvanesan, J.M. Babu, Impact of nano cerium oxide addition with pyrolysis waste plastic oil on combustion, performance and emission characteristics of CRDI diesel engine[J], Eng. Res. Express 6 (4) (2024) 045551.
[2] P. Akashkumar, C. Nagesh, J.M. Babu, et al., Production and engine performance and emission evaluation of karanja and Jatropha-Based Biodiesel[C]. Proceedings of the 19th Asia Pacific Automotive Engineering Conference & SAE-China Congress 2017: Selected Papers, 2018, pp. 1119–1133.
[3] M. Nagappan, J.M. Babu, In ternary blend fuelled diesel engines, nanoparticles are used as an additive in biofuel production and as a fuel additive: a review[J], Mater. Today Proc. (2023).
[4] M. Wang, X. Li, J. Su, et al., A study on the reasonable width of narrow coal pillars in the section of hard primary roof hewing along the air excavation roadway, J.]. Energy Sci. Eng. 12 (6) (2024) 2746–2765.
[5] M. Wang, J. Su, H. Qin, et al., Research on active advanced support technology of backfilling and mining Face[J], Rock. Mech. Rock. Eng. 57 (2024) 7623–7642.
[6] L. Zhang, L. Luo, J. Pan, et al., Seepage characteristics of coal under complex mining stress environment Conditions[J], Energy Fuels 38 (17) (2024) 16371–16384.
[7] Q. Niu, M. Hu, J. Chang, et al., Explosive fracturing mechanism in low-permeability sandstone-type uranium deposits considering different acidification reactions[J], Energy 312 (2024) 133676.
[8] B. Gan, Z. Li, W. Huo, et al., Phase transitions of CH4 hydrates in mud-bearing sediments with oceanic laminar distribution: mechanical response and stabilization-type evolution[J], Fuel 380 (2025) 133185.
[9] X. Fu, Z. Niu, C. Peng, et al., Quantitative synergistic adsorption affinity of Ca(II) and sodium oleate to predict the surface reactivity of hematite and quartz[J], Sep. Purif. Technol. 36 (3) (2025) 131196.
[10] C. Peng, X. Fu, Z. Niu, et al., Protonation behavior study of the active sites on typical sulfide minerals surface using surface complexation model[J], Colloids Surf. A Physicochem. Eng. Asp. 710 (2025) 136307.
[11] Q. Niu, X. Zhao, J. Chang, et al., Numerical simulation on physical composite stimulation and geothermal development performance of hot dry rock: a case study from matouying uplift, China[J], Appl. Therm. Eng. 267 (2025) 125714.
[12] X. Tan, X. Ma, X. Li, et al., An adsorption model considering fictitious Stress[J], Fractal Fract. 9 (1) (2025) 17.
[13] D. Khatri, A. Gopan, Z. Yang, et al., Characterizing early stage sub-micron particle formation during pulverized coal combustion in a flat flame burner[J]. Fuel 258 (2019) 115995.
[14] W.R. Seeker, G.S. Samuelsen, M.P. Heap, et al., The thermal decomposition of pulverized coal particles[J]. Symp Combust. 18 (1) (1981) 1213–1226.

[15] L.D. Timothy, D. Froelich, A.F. Sarofim, et al., Soot formation and burnout during the combustion of dispersed pulverized coal particles[J]. Symp Combust. 21 (1) (1988) 1141–1148.
[16] G. Fan, L. Hong, J. Luo, et al., Photocatalytic inactivation of harmful algae and degradation of cyanotoxins microcystin-LR using GO-based Z-scheme nano catalysts under visible light[J]. Chem. Eng. J. 392 (2020) 123767.
[17] X. Ran, D. Li, Y. Jian, et al., Fundamentals of coal topping gasification: characterization of pyrolysis topping in a fluidized bed reactor[J], Fuel Process. Technol. 91 (8) (2010) 810–817.
[18] G. Guan, C. Fushimi, A. Tsutsumi, Prediction of flow behavior of the riser in a novel high solids flux circulating fluidized bed for steam gasification of coal or biomass[J], Chem. Eng. J. 164 (1) (2010) 221–229.
[19] J. Zhang, Y. Wang, L. Dong, et al., Decoupling gasification: approach principle and technology Justification[J], Energy Fuels 24 (12) (2010) 6223–6232.
[20] W. Zhu, W. Song, W. Lin, Catalytic gasification of char from co-pyrolysis of coal and biomass[J], Fuel Process. Technol. 89 (9) (2008) 890–896.
[21] H.A. Dandajeh, N. Ladommatos, P. Hellier, et al., Effects of unsaturation of C_2 and C_3 hydrocarbons on the formation of PAHs and on the toxicity of soot particles[J], Fuel 194 (2017) 306–320.
[22] A.R. Gibbs, F.D. Pooley, Analysis and interpretation of inorganic mineral particles in "lung" tissues[J], Thorax 51 (3) (1996) 327–334.
[23] L. Morawska, J. Zhang, Combustion sources of particles. 1. health relevance and source signatures[J]. Chemosphere 49 (9) (2002) 1045–1058.
[24] Z. Zhao, J. Gao, Q. Du, et al., Effect of na on the condensation reaction of naphthalene molecules during coal pyrolysis[J], J. Energy Inst. 98 (2021) 313–321.
[25] X. Zhang, Feasibility on semicoke substitute for anthracite in energy conversion and emissions reduction[J], Clean. Coal Technol. 21 (3) (2015) 103–106.
[26] H. Katalambula, R. Gupta, Low-grade coals: a review of some prospective upgrading technologie[J], Energy Fuels 23 (7) (2009) 3392–-3405.
[27] G. Wang, Y. Wang, J. Lv, et al., Effect of red mud-based additives on the formation characteristics of tar and gas produced during coal pyrolysis[J], J. Energy Inst. 104 (2022) 1–11.
[28] W. Pan, M.A. Serageldin, Effect of calcium chloride and calcium acetate on the reactivity of a lignite coal at low heating rate[J], Thermochim. Acta 125 (1988) 285–294.
[29] S. Lin, M. Harada, Y. Suzuki, et al., Comparison of pyrolysis products between coal , coal / CaO , and coal / $Ca(OH)_2$ materials[J], Energy Fuels 17 (3) (2003) 602–607.
[30] S. Lin, Y. Suzuki, H. Hatano, et al., Developing an innovative method, HyPr-RING, to produce hydrogen from hydrocarbons[J], Energy Convers. Manag. 43 (9) (2002) 1283–1290.
[31] H. Liu, J. Zhou, J. Wang, Effects of Ca-based additves on behaviors of slow and fast coal pyrolysis[J], Mod. Chem. Ind. 31 (3) (2011) 70–72.
[32] H. Liu, The coal pyrolytic and gasification behaviors and sulfur transformation under the effect of Ca-based additives[D], University of Science and Technology, Shanghai: East China, 2011.
[33] Z. Liu, R. Wang, L. Ji, et al., Effect of calcium compounds on pyrolysis of coals[J], Journal Beijing University Chemical Technology (Natural Science) 42 (4) (2015) 1–9.
[34] P.J.A. Withers, J.J. Elser, J. Hilton, et al., Greening the global phosphorus cycle: how Green chemistry can help achieve planetary p sustainability[J], Green. Chem. 46 (23) (2015) 2087–2900.
[35] L. Reijnders, Phosphorus resources, their depletion and conservation, a review [J], Resour. Conserv. Recycl. 93 (2014) 32–49.
[36] H. Li, W. Ge, J. Zhang, et al., Control foaming performance of phosphate rocks used for wet-process of phosphoric acid production by phosphoric acid[J], Hydrometallurgy 195 (2020) 105364.
[37] S. Kounbach, M.B. Embarek, L. Mahi, et al., Simultaneous determination of H_2SiF_6, HF and total fluoride in fluorosilicic acid recovered from wet phosphoric acid production by potentiometric titration[J], Microchem. J. 175 (2022) 107152.
[38] M. Hang, F. Xiao, Z. Bo, Self-Anticorrosion for the combustion tower of heat recovered thermal process phosphoric acid Production[J], Process Saf. Environ. Prot. 118 (2018) 330–347.
[39] C. Zan, L. Shi, Y. Song, et al., Evaluation method for thermal processing of phosphoric acid with waste heat recovery[J], Energy 31 (14) (2006) 2791–2804.
[40] W. Li, H. Gao, Y. Luo, et al., Status trends and suggestions of phosphorus ore resources at home and abroad[J], China Min. Mag. 6 (24) (2015) 6–10.
[41] Q. Yang, S. Yang, C. Ma, et al., Effect of pretreatment on phosphate smelting reduction reaction[J], Ind. Miner. Process. 45 (12) (2016) 3–5.
[42] Z. Tian, B. Zhang, J. Yue, et al., Feasibility analysis and mechanism study of different sulfate waste residues for carbothermal reduction of phosphorite in a fluidized bed[J], J. Ind. Eng. Chem. 3 (2025).
[43] Z. Tian, Q. Wang, D. Ma, et al., Effect of aluminium sulfate on carbothermal reduction of phosphorite in a fluidized bed[J], J. Ind. Eng. Chem. 139 (2024) 138–148.
[44] W.S. Myung, D.B.N. Thanh, I.L. Young, et al., Solid circulation and loop-seal characteristics of a dual circulating fluidized bed: experiments and CFD simulation[J], Chem. Eng. J. 168 (2) (2011) 803–811.
[45] U. Hosanna, A. Kim, H. Kim, et al., CFD simulation of hydrodynamics and heat transfer characteristics in gas–solid circulating fluidized bed riser under fast pyrolysis flow condition[J], Appl. Therm. Eng. 212 (2022) 118555.
[46] 3558-1996 GB/T, Determination of chlorine in coal[S], Standards press of China, Beijing.
[47] S. Liaw, H. Wu, Leaching characteristics of organic and inorganic matter from biomass by water: differences between batch and semi-continuous operations[J], Ind. Eng. Chem. Res. 52 (11) (2013) 4280–4289.
[48] MT/T 1074-2007, Classification for alkali metal (potassium, sodium) content in coal [S], Standards press of China, Beijing.
[49] GB/T 20475.2-2006, Classification for content of harmful elements in coal - Part 2 : chlorine[S], Standards press of China, Beijing.
[50] R. Zhang, Experiments on sulfur transformation during coal pyrolysis combined with production of tar char and gas in double fluidized bed[D], Zhejiang University, 2021.
[51] M. Siyiti, Experimental research on the influence of atmosphere on pyrolysis characteristic during coal pyrolysis in fluidized bed reactor[D], Zhejiang University, 2018.
[52] K. Li, Research on coal pyrolysis-based technology co-producing tar char gas in dual fluidized beds with char heat carrier[D], Zhejiang University, 2022.
[53] R. Cao, Y. Li, J. Xia, et al., Silicon 1 (2019) 1–8.
[54] Z. Tian, Q. Wang, D. Ma, et al., Effect of aluminium sulfate on carbothermal reduction of phosphorite in a fluidized bed[J], J. Ind. Eng. Chem. 139 (2024) 138–148.
[55] GB/T 1871.1-1995, Phosphorite and concentrate–Determination of phosphrous pentoxide content–Quinoline phosphomolybdate gravimetric and volumetric methods[S], Standards press of China, Beijing.
[56] C. Wang, Y. Liu, D. Che, Experimental investigation on combustion characteristics of coal in low oxygen concentration[J], J. Eng. Thermophys. 31 (10) (2010) 1785–1788.
[57] M. Muthuraman, T. Namioka, K. Yoshikawa, Characteristics of co-combustion and kinetic study on hydrothermally treated municipal solid waste with different rank coals: a thermogravimetric analysis[J], Appl. Energy 87 (1) (2010) 141–148.
[58] Q. Wang, H. Wang, B. Sun, et al., Thermo-gravimetric study and kinetic analysis of blended combustion characteristics of oil shale and semi-coke[J], CIESC J. 58 (11) (2007) 2882–2888.
[59] J. Zhang, L. Chen, C. Wang, et al., Co-combustion characteristics and kinetic analysis of semi-coke and biomass in O_2/CO_2 atmosphere[J], Coal Convers. 3 (2024) 1–13.
[60] X. Huang, X. Jiang, X. Han, et al., Combustion characteristics of fine-and micropulverized coal in the mixture of O_2/CO_2[J], Energy Fuels 22 (6) (2008) 3756–3762.
[61] Y. Xie, J. You, M. Lu, et al., Raman spectroscopic study of coal samples during heating[J], Appl. Sci. 9 (21) (2019) 4699.
[62] J. Zhang, Z. Sun, Q. Guo, et al., Structural changes of shenfu coal in pyrolysis and hydrogasification reactivity of the char[J], J. Fuel Chem. Technol. 45 (2) (2017) 129–137.
[63] H. Zhao, Y. Li, Y. Shu, et al., Effect of calcium oxide on pyrolysis products distribution and char structure of lignite and anthracite[J], Coal Sci. Technol. 44 (3) (2016) 177–183.
[64] X. Zhang, C. Zou, J. Zhao, et al., Effect of H_2 and CO as pyrolysis atmosphere on chemical structure of char by XRD and Raman methods[J], J. Fuel Chem. Technol. 47 (11) (2019) 1288–1297.
[65] Y. Xu, X. Chen, L. Wang, et al., Progress of Raman spectroscopic investigations on the structure and properties of coal[J], J. Raman Spectrosc. 51 (9) (2020) 1874–1884.
[66] E. Quirico, N. Rouzaud, L. Bonal, et al., Maturation grade of coals as revealed by Raman spectroscopy: progress and problems[J], Spectrochim. Acta Part A Mol. Biomol. Spectrosc. 61 (10) (2005) 2368–2377.
[67] D.M. Quyn, H. Wu, C. Li, Volatilisation and catalytic effects of alkali and alkaline earth metallic species during the pyrolysis and gasification of victorian brown coal. Part I. Volatilisation of na and cl from a set of NaCl-loaded samples[J], Fuel 81 (2) (2002) 143–149.
[68] H. Tay, S. Kajitani, S. Wang, et al., A preliminary Raman spectroscopic perspective for the roles of catalysts during char gasification[J], Fuel 121 (2014) 165–172.
[69] V.I. Stenberg, M.B. Jones, N.J. Suwarnasarn, Radicals in coals during pyrolysis in relation to liquefaction conversion[J], Fuel 64 (4) (1985) 470–474.
[70] B. Delley, From molecules to solids with the $DMol^3$ approach[J], J. Chem. Phys. 113 (2000) 7756–7764.
[71] J.P. Perdew, K. Burke, M. Ernzerhof, Generalized gradient approximation made simple[J], Phys. Rev. Lett. 77 (1996) 3865–3868.
[72] M. Methfessel, A.T. Paxton, High-precision sampling for Brillouin-zone integration in metals[J], Phys. Rev. B 40 (1989) 3616–3621.
[73] L. Zheng, J. Jin, R. Zhang, et al., Understanding the effect of dolomite additive on corrosion characteristics of straw biomass ash through experiment study and molecular dynamics calculations[J], Energy 271 (2023) 126950.
[74] J.K. Christie, R.I. Ainsworth, N.H. de Leeuw, Ab initio molecular dynamics simulations of structural changes associated with the incorporation of fluorine in bioactive phosphate glasses[J], Biomaterials 35 (24) (2014) 6164–6171.
[75] B. Pan, H. He, Molecular dynamics simulations of the metallic behavior of the si (0 0 1) surface at high temperatures[J], Phys. Rev. B 77 (11) (2008) 113302.
[76] F.J. Spera, D. Nevins, M. Ghiorso, et al., Structure, thermodynamic and transport properties of CaAl2Si2O8 liquid. Part I: molecular dynamics simulations[J], Geochim. Et. Cosmochim. Acta 73 (22) (2009) 6918–6936.
[77] L. Zheng, J. Jin, R. Zhang, et al., Understanding the effect of dolomite additive on corrosion characteristics of straw biomass ash through experiment study and molecular dynamics calculations[J], Energy 271 (2023) 126950.
[78] K.D. Nishith, S. Tetsuo, T. Yoichi, A fundamental study of Fe-Cr binary alloy-oxide film interfaces at 288 °C by computational chemistry calculations[J], Corros. Sci. 52 (7) (2010) 2349–2352.

[79] J. Pak, I. Kim, R. Kim, et al., Surface energy and its anisotropy for fcc metals: modified embedded atom method study[J], Indian J. Phys. 97 (2023) 1981–1988.
[80] E. Hu, X. Zeng, D. Ma, et al., Effect of the moisture content in coal on the pyrolysis behavior in an indirectly heated Fixed-Bed reactor with internals, J.]. Energy Fuels 31 (2) (2017) 1347–1354.
[81] Z. Wu, W. Yang, Y. Li, et al., Co-pyrolysis behavior of microalgae biomass and low-quality coal: products distributions, char-surface morphology, and synergistic effects[J], Bioresour. Technol. 255 (2018) 238–245.
[82] Y. Jia, J. Huang, Z. Cheng, et al., Effect of CaO on tar cracking in a rapid-pyrolysis fixed bed reactor[J], Coal Convers. 24 (2) (2011) 53–57.
[83] C. Li, C. Sathe, J. Kershaw, et al., Fates and roles of alkali and alkaline earth metals during the pyrolysis of a victorian brown coal[J]. Fuel 79 (3) (2000) 427–438.
[84] C. He, X. Min, H. Zheng, et al., Study on the volatiles and kinetic of in-Situ catalytic pyrolysis of swelling Low-Rank Coal[J], Energy Fuels 31 (12) (2017) 13558–13571.
[85] C. Ma, Y. Zhao, T. Lang, et al., Pyrolysis characteristics of low-rank coal in a low-nitrogen pyrolysis atmosphere and properties of the prepared chars[J], Energy 277 (2023) 127524.
[86] Y. You, Z. Zheng, R. Wang, et al., Numerical study on combustion behavior of Semi-Coke in blast furnace Blowpipe-Tuyere-Combustion Zone[J], Metals 12 (8) (2022) 1272.
[87] Y. Zhang, N. Gao, C. Quan, et al., Study on structural properties of semi-coke from pulverize coal pyrolysis and influencing factors during its thermal transportation process[J], J. Anal. Appl. Pyrolysis 173 (2023) 106052.
[88] L. Ge, C. Zhao, S. Chen, et al., An analysis of the carbonization process and volatile-release characteristics of coal-based activated carbon[J], Energy 257 (2022) 124779.
[89] J. Zhang, J. Wang, Z. Li, et al., Molecular dynamics simulation and gas generation tracking of pyrolysis of bituminous Coal[J], ACS Omega 7 (13) (2022) 11190–11199.
[90] Q. Wang, Z. Hua, J. Guan, Structure of wangqing oil shale and mechanism of carbon monoxide release during its pyrolysis[J], Energy Sci. Eng. 7 (6) (2019) 2398–2409.
[91] M. Niu, L. Xin, W. Cheng, et al., Effects of pressurized pyrolysis on the chemical and porous structure evolution of coal core during deep underground coal Gasification[J]. ACS Omega 8 (43) (2023) 40153–40161.
[92] B. Tian, Y. Qiao, J. Fan, et al., Coupling pyrolysis and gasification processes for Methane-Rich syngas production: fundamental studies on pyrolysis behavior and kinetics of a Calcium-Rich High-Volatile bituminous Coal[J], Energy Fuels 31 (10) (2017) 10665–10673.
[93] L. He, S. Zhang, Q. Yao, et al., A review of catalytic conversion of coal tar value-added chemicals at the molecular level based on first principles[J], Energy Convers. Manag. 326 (2025) 119466.
[94] D. Wu, S. Zhang, Q. Zheng, et al., The influence of CaO on the pyrolysis behavior and kinetic characteristics of low rank Coal[J], Energy Procedia 105 (2017) 2039–2046.
[95] Q. Lu, N. Zhang, Q. Yang, et al., Influence of calcium promoter on catalytic pyrolysis characteristics of iron-loaded brown coal in a fixed bed reactor[J], J. Energy Inst. 93 (2) (2020) 695–710.
[96] L. Liu, H. Liu, M. Cui, et al., Calcium-promoted catalytic activity of potassium carbonate for steam gasification of coal char: transformations of sulfur[J], Fuel 112 (2013) 687–694.
[97] J. Xu, S. Su, Z. Sun, et al., Effects of steam and CO_2 on the characteristics of chars during devolatilization in oxy-steam combustion process[J], Appl. Energy 182 (2016) 20–28.
[98] Z. Tian, Q. Wang, Investigation of the products and the migration of sodium and chlorine during pyrolysis of high-Sodium coal mixed with phosphorite[J], AsiaPac. J. Chem. Eng. 3183 (2024).
[99] M. Ma, Y. Bai, J. Wei, et al., Molecular dynamics simulations and experimental study on deconvolution of volatile-char interaction in coal pyrolysis: insight into the role of O-containing compound species[J], Chem. Eng. Sci. 277 (2023) 118874.
[100] J. Zhang, Z. Sun, Q. Guo, et al., Structural changes of shenfu coal in pyrolysis and hydrogasification reactivity of the char[J], J. Fuel Chem. Technol. 45 (2) (2017) 129–137.
[101] X. Li, J. Hayashi, C. Li, FT-Raman spectroscopic study of the evolution of char structure during the pyrolysis of a victorian brown coal[J]. Fuel 85 (12-13) (2006) 1700–1707.
[102] H. Tay, S. Kajitani, S. Zhang, et al., Effects of gasifying agent on the evolution of char structure during the gasification of victorian brown coal[J], Fuel 103 (2013) 22–28.
[103] Z. Tian, B. Zhang, Q. Wang, et al., Investigation of product properties and reaction mechanism of low-rank coal pyrolysis with phosphorite in a fluidized bed[J], J. Environ. Chem. Eng. 13 (2) (2025) 115559.
[104] Y. Yang, J. Liu, J. Wang, et al., Effect of the pyrolysis temperature on the grindability of Semi-cokes produced by two kinds of Low-Rank Coalss[J], Energy Fuels 32 (2) (2018) 1297–1308.
[105] B. Wang, L. Sun, S. Su, et al., Char structural evolution during pyrolysis and its influence on combustion reactivity in air and oxy-fuel conditions[J], Energy Fuels 26 (3) (2012) 1565–1574.
[106] W. Wang, R. Lemaire, A. Bensakhria, et al., Review on the catalytic effects of alkali and alkaline earth metals (AAEMs) including sodium, potassium, calcium and magnesium on the pyrolysis of lignocellulosic biomass and on the co-pyrolysis of coal with biomass[J], J. Anal. Appl. Pyrolysis 163 (2022) 105479.
[107] S. Rodrigues, I. Suárez-Ruiz, M. Marques, et al., Catalytic role of mineral matter in structural transformation of anthracites during high temperature treatment[J], Int. J. Coal Geol. 93 (2012) 49–55.
[108] M. Chen, C. Cai, J. Bao, et al., Effect of aliphatic segment length and content on crystallization and biodegradation properties of aliphatic-aromatic co-polyesters [J], Polym. Degrad. Stab. 203 (2022) 110080.
[109] L.S. Figueroa, C.A. Guymon, Aliphatic chain length effects on photopolymerization kinetics and structural evolution of polymerizable lyotropic liquid crystals[J], Polymer 49 (9) (2008) 2260–2267.
[110] C. Wang, X. Jin, Yi Wang, et al., Release and transformation of sodium during pyrolysis of zhundong coals, J.]. Energy Fuels 29 (1) (2015) 78–85.
[111] L. Xu, H. Liu, D. Zhao, et al., Transformation mechanism of sodium during pyrolysis of zhundong coal[J], Fuel 233 (2018) 29–36.
[112] D. Ma, R. Li, X. Wang, et al., Chlorine evolution and char characteristics during pyrolysis upgrading of xinjiang high chlorine coal[J], Fuel 379 (2025) 133120.
[113] R. Cao, J. Xia, W. Li, et al., Effects of alkali metal carbonates on carbothermal reduction of phosphate Rock[J], J. Chem. Eng. Chin. Univ. 32 (3) (2018) 568–576.
[114] Q. Yang, S. Yang, C. Ma, Application of mixed collectors in direct flotation test of cellophane[J], Ind. Miner. Process. 45 (12) (2016) 3–5.
[115] X. Li, R. Huang, Q. Wu, et al., Experimental approach for the characterization of Low-Grade phosphate ore performance in isothermal Conditions[J], J. Sustain. Metall. 7 (2021) 1736–1747.
[116] M. Li, R. Zhu, R. Huang, et al., Effect of MgO on vacuum carbothermal reduction mechanism of $Ca_3(PO_4)_2$ in SiO_2-C-$Ca_3(PO_4)_2$-MgO-Based System[J], J. Sustain. Metall. 9 (2023) 1429–1443.
[117] J. Men, Y. Li, P. Cheng, et al., Recycling phosphogypsum in road construction materials and associated environmental considerations: a review[J], Heliyon 8 (11) (2022) 11518.
[118] Q. Wu, J. Li, X. Lv, et al., Reaction mechanism of Low-Grade phosphate ore during vacuum carbothermal Reduction[J], Metall. Mater. Trans. B 52 (2021) 1484–1494.
[119] N. Alimatun, I. Inggrid, N.P. Adeline, et al., Carbon footprint analysis on phosphoric acid production using wet process at PT petrokimia Gresik[C], in: The 10th International Conference on Engineering, Technology, and Industrial Application, 517, 2024, p. 08005.
[120] M. Pang, Z. Sun, M. Chen, et al., Influence of phosphorus slag on physical and mechanical properties of cement Mortars[J], Materials 13 (10) (2020) 2390.
[121] Y. Ban, L. Jin, J. Zhu, et al., Insights into effect of $Ca(OH)_2$ on pyrolysis behaviors and products distribution of hongshaquan coal[J], Fuel 307 (2022) 121791.
[122] J. Shang, W. Guo, P. Yang, et al., Catalytic fast pyrolysis of Tar-Rich coal with a bauxite residue for upgrading High-Value products: product distribution and kinetic Analysis[J], ACS Omega 9 (25) (2024) 26911–26921.
[123] X. Cheng, X. He, C. Chen, et al., Influence of Fe_2O_3/CaO catalysts on the pyrolysis products of Low-Rank Coal[J], Energy Technol. 3 (10) (2015) 1068–1071.
[124] Y. Zhang, G. Chen, L. Wang, et al., Microwave-Assisted pyrolysis of Low-Rank coal with K_2CO_3, $CaCl_2$, and $FeSO_4$ Catalysts[J], ACS Omega 5 (28) (2020) 17232–17241.